August 2017

An Array of Circular Dielectrophoresis Traps to Separate and Charaterize Individual Microparticles from Population

Hwangjae Lee
University of Wisconsin-Milwaukee

AN ARRAY OF CIRCULAR DIELECTROPHORESIS TRAPS TO SEPARATE AND CHARATERIZE INDIVIDUAL MICROPARTICLES FROM POPULATION

by

Hwangjae Lee

A Thesis Submitted in

Partial Fulfillment of the

Requirements for the Degree of

Master of Science

in Engineering

at

The University of Wisconsin-Milwaukee

August 2017

ABSTRACT

AN ARRAY OF CIRCULAR DIELECTROPHORESIS TRAPS TO SEPARATE AND CHARATERIZE INDIVIDUAL MICROPARTICLES FROM POPULATION

by

Hwangjae Lee

The University of Wisconsin-Milwaukee, 2017
Under the Supervision of Professor Woo-Jin Chang

Dielectrophoretic traps have been broadly studied in light of their many advantages of high controllability, ease of operation, and high efficiency. In the previous studies, however, it was challenging to count captured particles or required work to capture particles. In the thesis, an array of circular dielectrophoresis (DEP) traps was developed and tested to manipulate population of microparticles in single particle level. The circular DEP traps enable more precise control of the force field than conventionally used interdigitated electrodes due to its omnidirectional and symmetric properties. The location of the captured microparticle inside the trap was confirmed by both of numerical and experimental approaches, based on the direction and amplitude of the force field generated by numerical simulation. This comprehensive analysis facilitated separation as well as trapping. The individual microparticle captured in separate trap can be further tested or treated by follow up treatments.

To

my all family members, friends,

and Republic of Korea Army.

TABLE OF CONTENTS

LIST OF FIGURES

LIST OF TABLES

LIST OF ABBREVIATIONS

DEP	Dielectrophoresis
LOC	Lab-on-a-Chip
CM	Clausius-Mossotti
IDT	Interdigitated
ITO	Indium Tin Oxide
FEM	Finite Element Method
CAD	Computer Aided Design
UV	Ultra Violet
HMDS	Hexamethyldisilazane
DI	Deionized Water
MEMS	Micro-Electro-Mechanical System

ACKNOWLEDGEMENTS

First, I would like to thank my advisor, Dr. Woo-Jin Chang for trusting my ability and understanding my situation. He has not only helped me to widen my perspective in engineering but also given me a priceless chance to explore the U.S. I would have felt something missing if he were not my advisor. It was one of the luckiest things to become a part of his research members on this journey. My co-worker, Tae Joon Kwak, can't be missed. What he has done for me is tremendous. All his support as a co-worker and a friend has helped me get through obstacles I have encountered not only in the academic area but in personal life. I hope he would finish his study successfully and become a great scientist that he wants to be. I am sure he will. I also thank Mohammad Rizwen Ur Rahman for being a nice companion. He has made my study here in UW-Milwaukee more energetic and memorable. It's not finished yet. We will have more wonderful memories until saying good bye.

A tremendous thanks to Dr. Jörg C. Woehl and Dr. Ilya V Avdeev for being the members of my thesis committee. I appreciate their time to evaluate my work. I also appreciate all the efforts that professors and TAs made for me in the classes I took. Last but not least, I thank Republic of Korea Army for giving me such a wonderful and valuable chance. In the first place, this would not have happened without my country and the Army. I look forward to the military service I would do for my country.

Chapter 1

Introduction

1.1 Organization of the thesis

The work performed in this thesis focuses on trapping single particles using an array of dielectrophoretic trap. The fabrication and numerical simulation of electrical dielectrophoresis (DEP) trap are illustrated in detail. The reasons why this trap is optimized for quantifying physical properties of single particle is also demonstrated.

Chapter 1 presents the theory and experimental designs for the most significant approaches to DEP traps including its application areas. Chapter 2 is based on the fabrication of DEP trap device and the general experimental setup. Numerical simulation of the electrical DEP trap is introduced, which leads to DEP force simulation. Chapter 3 presents trapping experiments using different sized of polystyrene beads and traps including its numerical simulation. Chapter 4 features the effect of spacer is demonstrated with the details of the DEP trap's electrical and physical properties. Chapter 6 consists of conclusion and future direction of the DEP trap's application.

1.2 Particle trapping and separation

In the last several decades, a variety of methods have been studied and used widely to trap, manipulate, separate and concentrate particles. Systems designed for these purposes in many areas have improved both in quality and in efficiency. Typical methods of these systems include mechanical [1], optical [2], microfluidic [3], and magnetic [4] manners. Due to improvement of theses particle control skills, its application has also spread to a various areas such as bioscience [5], biomedical [6] and dental sciences fields [7].

1.3 Dielectrophoresis (DEP) theory and trap

The phenomenon of DEP was first observed by Reuss F during his study of clay particles. After Reuss's discovery, several researches about revealing the characteristics of DEP were conducted by Pohl who named this phenomenon as "dielectrophoresis" [8], [9].

A non-uniform electric field and polarizable particles are the main factor to generate a DEP force. When dielectric particles are suspended in non-uniform electric field, a DEP force affects those particles [10]. The relative polarizabilities of the particle and of the surrounding medium determines the magnitude and direction of the DEP force [11]. For a spherical particle of radius r, the DEP force is defined as:

$$< \vec{\mathrm{F}} > = 2\pi r^3 \varepsilon_o \varepsilon_m Re[K(\omega)] \nabla E^2 \tag{1}$$

where ε_o is the permittivity of free space, ε_m is the permittivity of the surrounding medium, and r is the particle radius. ∇E^2 denotes the electric field gradient and $Re[K(\omega)]$ is the Clausius-Mossotti factor. The Clausius-Mossotti factor is defined as follows:

$$\mathrm{K}(\omega) = \frac{\varepsilon_p^* - \varepsilon_m^*}{\varepsilon_p^* + 2\varepsilon_m^*} \tag{2}$$

ε^* in Equation (2) is the complex permittivity and subscripts p and m stand for the particles and the medium, respectively. The complex permittivity ε* is described as follows:

$$\varepsilon^* = \varepsilon - j\frac{\sigma}{\omega} \tag{3}$$

where ε is the permittivity, σ is the conductivity, $j = \sqrt{-1}$, and ω is the angular frequency of the applied AC electric field.

Particles exhibit either a positive DEP (p-DEP) or a negative DEP (n-DEP) depending on the real part of $K(\omega)$, which is expressed as $Re[K(\omega)]$. This value is bounded by the limits -0.5 < $Re[K(\omega)]$ < 1 for spherical particles and it depends on the frequency of the applied electric field and the relative magnitudes of ε_p^* and ε_m^* [12]. By controlling these parameters, particles can be led to a wanted direction, which enables separation and manipulation of particles. Positive DEP occurs when the complex permittivity of the particle is higher than that of the surrounding medium, $\varepsilon_p^* > \varepsilon_m^*$, and it results to $Re[K(\omega)] > 0$. Particles under positive DEP has a tendency to travel towards to the higher electric field gradient region such as electrode edges. On the other hand, when the complex permittivity of the medium is higher than that of the particle, $\varepsilon_m^* > \varepsilon_p^*$, or $Re[K(\omega)] < 0$, particles experience negative DEP. Under the effect of negative DEP, particles travel towards the low electric field gradient region [13].

Interdigitated (IDT) electrodes have been frequently studied for DEP force in the last several decades. In most cases of IDT electrodes, the electric field gradient is higher at the electrode edges compared to the center of the electrodes and the gap between the electrodes. When the system is affected by positive DEP, particles are attracted to the edges of the interdigitated electrodes due to its high electric field gradient. On the contrary, particles are repelled away from the edges and move towards the point where has low electric field gradient under negative DEP [1], [5]. Figure 1 illustrates the movements of the particles depending on their state including a normal state.

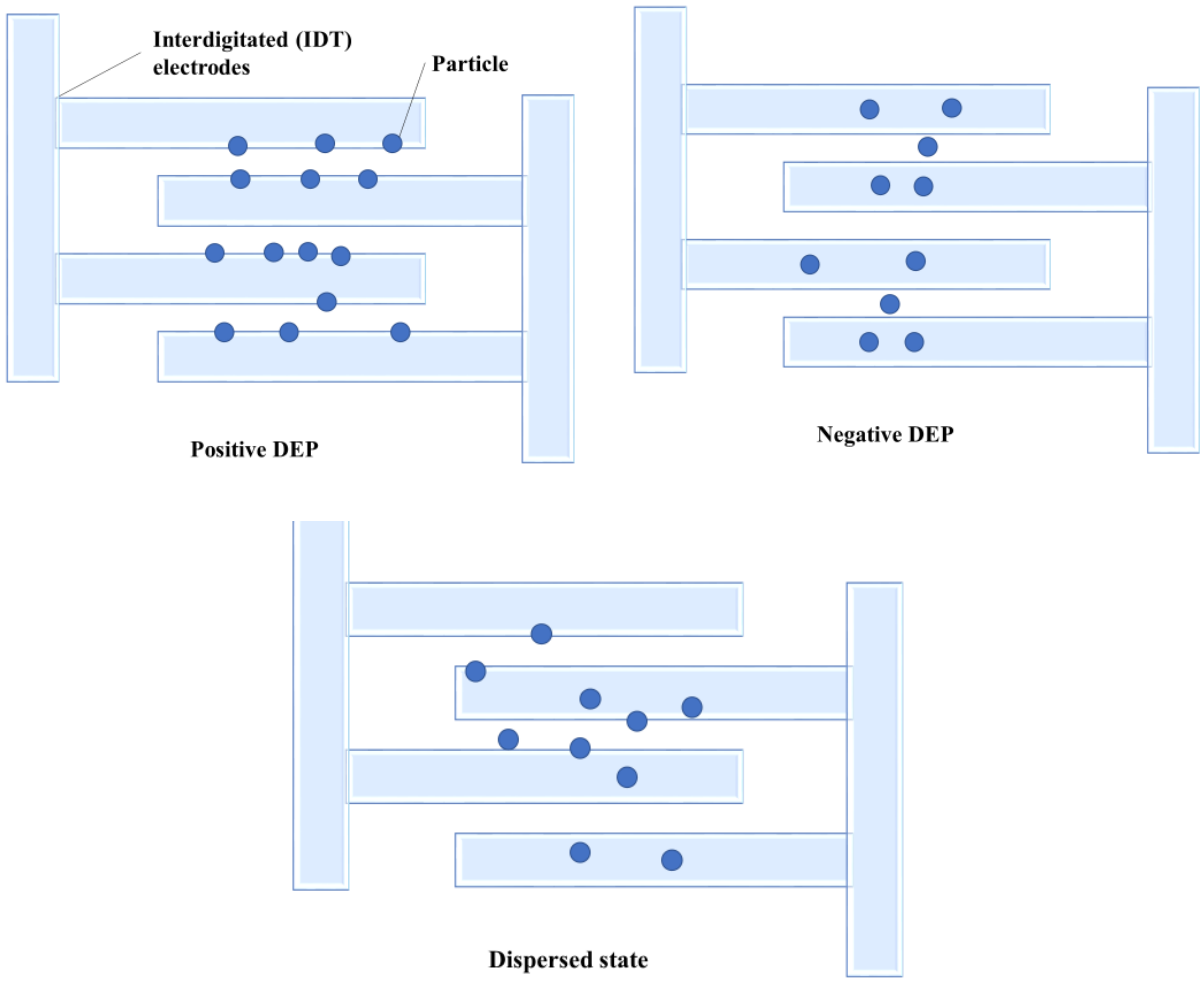

Figure 1. A schematic illustration of the responses of polarizable particles under interdigitated (IDT) electrodes. Under positive DEP, particles travel towards to the electrode edges where the electric field maxima. Particles are repelled away from the electrodes and move towards the point where has low electric field gradient under negative DEP. In this case, the low electric field gradient is generated both in the middle of electrodes and in the gap between the electrodes.

Even though a variety of methods have been studied and used widely to trap, manipulate, separate and concentrate particles, DEP has been considered the optimized method for

electrically neutral particles with strong controllability, easy operation, high efficiency, low cost and slight damage compared to other methods [15]. Optical method is not the best because of hard operation and high cost; microfluidic method has a weak controllability; large damage is hard to avoid in mechanical method; magnetic method also has a disadvantage of hard operation.

In recent times, the improvement of Micro-Electro-Mechanical System (MEMS) technology has enabled fabrications of lab-on-a-chip for DEP to be easier and effective. Many researches to maximize the benefits of DEP such as easy fabrication, strong controllability have been studied. DEP has been used in capturing and controlling bacteria [16], viruses [17], DNA [18], yeast cells [19], parasites [20], sperm cells [21] and cancer cells [22].

Design of electrodes in DEP play an important role in characterizing a purpose of system with the types of DEP such as positive and negative DEP. In general, electrode structures can be classified into planar and three-dimensional (3D) categories. Electrodes of planar design are broadly used with easiness of fabrication by utilizing lithography procedures on top of a microchannel [10]. Spiral [23], curved [14], matrix [24], interdigitated [25], and oblique [26] shapes of electrodes has been fabricated and studied. 3D electrodes can be fabricated in more different ways than planar electrodes. However, 3D electrodes fabrication process is complicated and needs more efforts. Extruded patterns [27], a sidewall pattern [28], a top-bottom pattern [29], micro wells [30], and DEP wells [31] have been fabricated using this method.

1.4 An array of circular DEP traps to characterize individual microparticle

A variety of planar electrode shapes in DEP traps such as Spiral [23], curved [14], matrix [24], interdigitated [25], and oblique [26] shapes of electrodes have been demonstrated. IDT electrode are widely used among them with easiness of collecting particles [32], [33]. However,

IDT electrode is not optimized for analyzing in a single particle level, while it is suitable for manipulating a large number of particles. In addition to that, the location of particles under negative DEP in IDT electrode can't be predictable because it can be trapped either on the center of the electrodes or on the gap between the electrode as shown in Figure 1.

In most case of circle shaped electrodes, however, particles are attracted to the edges of the circle shaped electrodes due to its high electric field gradient under positive DEP. In the opposite, particles are repelled away from the electrodes and move towards the point that has low electric field gradient under negative DEP. This circular DEP trap can avoid the IDT electrode's uncertainty under negative DEP. Figure 2 illustrates the movements of the particles depending on their state including a normal state.

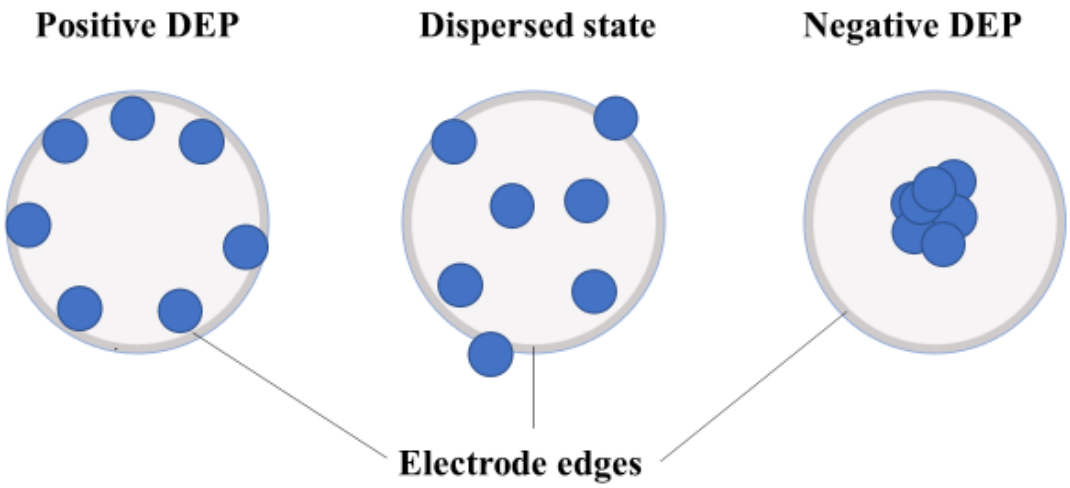

Figure 2. A schematic illustration of the responses of polarizable particles under circle shaped electrodes. Under positive DEP, particles travel towards to the electro edges where the electric field maxima. Particles are repelled away from the electrodes and move towards the center of the circular trap under negative DEP. This circular electrode design enables to avoid uncertainty that IDT electrode has under negative DEP.

Due to this stable and predictable property compared to IDT electrode, enclosed shape of electrodes have been introduced in a few researches to supplement the disadvantages of IDT electrode [10], [30], [34], but the geometry of electrodes in these researches is not perfect circle shape because of a long and narrow rectangular electrode attached to the end of the circle electrode.

This disadvantage was completely overcome with a perfect circular geometry array of DEP traps in our study, which results in a more stable electric field and DEP force. With omnidirectional property of the circle shaped DEP traps, this stableness facilitates matching experimental results of the DEP trap with results from numerical methods.

Trapping and separating a single particle has also been challenging for the past several decades under the DEP research areas even though the importance of fine-scale manipulation and positioning of single micro scale particles has been increasing because the applications in life science, diagnostic and medical industries have expanded.

DEP force has been used in many areas to capture and manipulate a large numbers [32], [35] of particles in light of many advantages of high controllability, ease of operation, and high efficiency, but not many researches have focused on DEP traps in a single particle level. Some of researches demonstrates capturing a single particle. However, those researches are confined to concentrating or immobilizing a stationary single particle [30], [34].

In the thesis, an array of circular DEP traps was developed and tested to manipulate population of microparticles in single particle level. The circular DEP traps enable more precise control of the force field than conventionally used IDT electrodes due to its omnidirectional and

symmetric properties. The location of the captured microparticle inside the trap was confirmed by both of numerical and experimental approaches, based on the direction and amplitude of the force field generated by numerical simulation.

As shown in Figure 3, the newly designed array of DEP traps in this thesis can capture and immobilize moving micro scale single particles in each trap. The velocities and particle's sizes that are required to be captured can be controllable with applied voltages and trap sizes. This novel property of the traps suggests the possibility of selective moving particle capturing. The DEP traps also facilitate analyzing each particle's individual physical characteristics. In addition, the inner hollow design of the traps enables observing particle's movements without any extra treatment such as fluorescence.

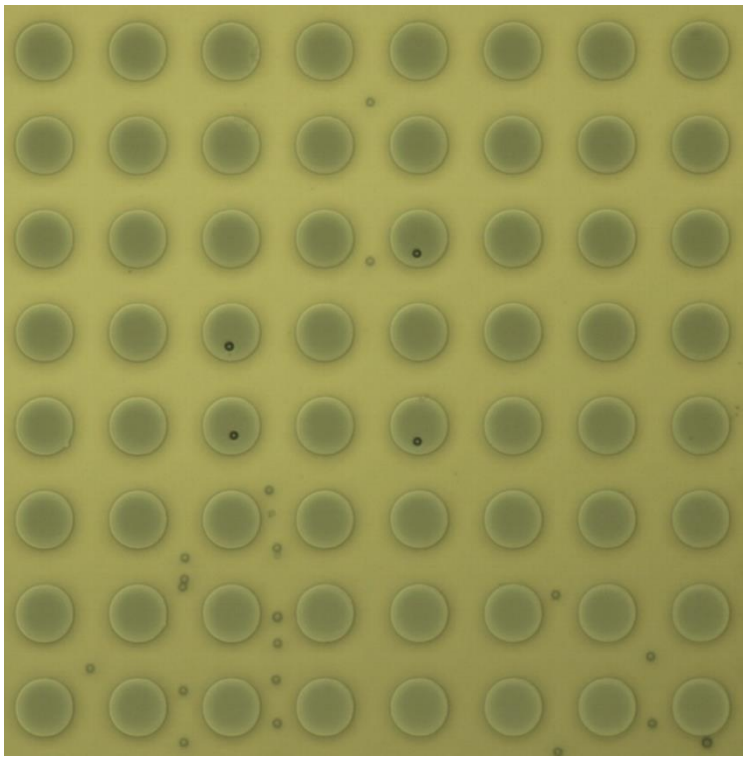

Figure 3. An array of 30 μm circle shaped electric DEP traps. Four polystyrene particle are captured in the middle of the array under negative DEP force. The circle shaped traps are transparent as opposed to the rest of area where chrome metal is deposited. Judging by the

position of particles which are close to the south rim of traps, it can be assumed that the medium is flowing from north to south direction.

The suggested traps supplement disadvantages of different shaped DEP traps and strengthen established single particle capturing skills in company with decreasing time and work that needed to fabricate DEP traps. Especially, the suggested array of DEP traps in this thesis focus on capturing and analyzing particle in a single particle level, while most researches have focused on manipulating a large number of particles [10], [34]. The DEP traps are also optimized to be numerically analyzed by eliminating unnecessary electrodes which may cause electric field or DEP force to be unstable. This numerical analysis enable to quantify physical properties of single particles in conjunction with experimental analysis. In addition to that, capturing and analyzing a moving single particle are demonstrated compared to many other researches [3], [30], [36], [37] which mainly demonstrate controlling a stationary single particle.

This thesis demonstrates that moving micro scale particles are captured according to their velocities and sizes by controlling applied voltages and trap sizes. Using this novel property, different sized particles can be separated. Spacer that is used to make a channel of particles between the microarray electrode on the bottom layer and the Indium Tin Oxide (ITO) counter electrode is also subject to change in order to see the different effect of the depth of spacer.

Each operation condition is generated by finite element method (FEM) using computer software (COMSOL Multiphysics V5.2). This work facilitates acquiring and quantifying the data related to particle's physical properties, which lead to the comprehensive and complete analysis of the system.

Chapter 2

Materials and Methods for Electrical DEP Trap

2.1 Overview

Planar geometry electrodes in microfluidic device have many advantages over 3D electrodes. One of the most competitive and crucial advantages is the easiness of fabrication. It's also cost-effective due to its short and convenient process. There are a variety methods for the fabrication of microfluidic devices such as reactive ion etching, wet etching, plasma etching, injection molding, conventional machining, hot embossing, and soft lithography [38]. Photolithography is regarded as a solid and fundamental process among all these methods [13]. Two-dimensional microelectrodes can be simply fabricated using photolithography process compared to other manners. The simplicity can minimize any experimental errors that can be caused from mistakes of fabrication.

In this chapter materials, equipment, and experimental methods for fabrication of an array of DEP traps to quantify physical properties of single particles will be discussed in detail. Photolithography technique was applied for the process of fabrication because of the benefits mentioned above. Numerical simulation of the array of electrical DEP trap were also conducted using computer simulation (COMSOL Multiphysics V5.2) to verify the validity of the experiment and quantify physical properties of single particles captured in the traps. Every detail from governing equations to geometry to mesh will be discussed.

2.2 Fabrication of DEP Trap Device

Prior to the process of photolithography, the circular electrode geometry was designed using the computer-aided design software (Auto CAD). Pure circle shaped geometry without any other extra electrode that attached to the circle was created and designed. As mentioned in the

introduction, the omnidirectional property of the circle shaped DEP traps facilitates matching experimental results of the DEP traps with results from numerical methods. Pure circle shaped design also contributes to producing a predictable and stable numerical simulation.

The circular electrode geometry designed by Auto CAD were used to make a photomask which can be reusable. A variety of arrays are engraved in the photomask; 10 μm diameter circle shaped traps with 10 μm gap between the traps, 20 μm diameter traps with the same gap, 30 μm diameter traps, and 40 μm diameter traps; Each size of traps from 10 μm to 40 μm are also designed with the different gaps sized from 10 μm to 50 μm. In this thesis, 10 μm ~ 40 μm traps with 20 μm gap and 40 μm traps with 40 μm gap were used.

Since the photomask can be reusable, only the photolithography and metal deposit processes were conducted each time new devices were needed. The brief procedures of the photolithography and metal deposit is referenced in Table 1.

Step	Process	Actions	Equipment
1	Preparation	Cut a 3 × 1" microscope slide glass into three pieces, then wash off with DI H_2O.	Glass cutter
2	Surface cleaning	Soak the slides in acetone, then sonicate it for 5 minutes. After rinsing it with methanol, soak the slides in methanol and sonicate it for 5 minutes again. At last, mix sulfuric acid and hydrogen peroxide for piranha cleaning, then soak the slides in the mixed solution for 30 minutes.	Sonicator

3	Baking	Place the slides on a convection oven for 5 minutes at 65℃.	Convection oven
4	Surface treatment	Put a small petri dish at the bottom of a vacuum chamber with 8 ~ 9 drops of hexamethyldisilazane (HMDS) in it. Then, place the slides on the rack of the vacuum chamber and vacuum for 5 minutes. After 5 minutes, stop vacuuming and let it still for 7 minutes.	Vacuum chamber
5	Photoresist coating	Coat the slides with a photoresist (AZ-5214) using a vacuum spin coater.	Spin coater
6	Baking	Place the slides on a hotplate for 5 minutes at 65℃.	Hotplate
7	UV exposure	Expose the slides to UV light with the photomask on it for 14 seconds at 7 mw/cm^2.	UV mask aligner
8	Developing	Mix the developer solution with DI H_2O at the ratio of 1:4. Soak and stir the slides for 55 seconds.	Beaker
9	Baking	Place the slides on a convection oven for 5 minutes at 65℃.	Convection oven
10	Metal deposit	Deposit pure chrome metal piece with purity 99% on the slides until the thickness of 1 K$\dot{A}$ at the rate of 0.1 ~ 0.3 $\dot{A}$/s.	Thermal evaporator
11	Lift-off	Soak the slides into acetone and sonicate it for 30 seconds.	Sonicator
12	Completion	Rinse the slides with DI H_2O and air dry with N_2 gas before use.	Convection oven

Table 1. The procedures and needed equipment for fabricating the array of circle shaped DEP traps.

2.2.1 Preparation and cleaning

The purpose of cleaning is to remove any contaminants on the material's surface which may affect the results of experiments. In addition, surface treatment is needed before photoresist coating to change the property of the surface from hydrophilic to hydrophobic, which can help coat photoresist. In this experiment, both solvent cleaning and piranha cleaning were used. The detail procedures and used materials from preparation to cleaning is as follows:

1) Preparation slides for the device
    a) Cut a 3 × 1" microscope slide glass (NO. 7101, Viomed, China) with a glass cutter into three pieces. Each slide becomes 1 × 1" size.
    b) Rinse with DI H_2O and air dry with N_2 gas
2) Solvent cleaning
    a) Soak the 1 × 1" size slides in acetone (NO. 841502, Carolina, USA) on a petri dish
    b) Sonicate for 5 minutes using a sonicator (2510R-MT 2510, Branson, USA)
    c) Rinse with methanol then, soak the slides in methanol
    d) Sonicate for 5 minutes
    e) Rinse with DI H_2O and air dry with N_2 gas
3) Piranha cleaning
    a) Mix 99 % sulfuric acid (NO. 893302, Carolina, USA) with 3 % hydrogen peroxide (NO. 858122, Carolina, USA) in a bowl at the ratio of 1:1
    b) Soak the slides in the mixed solution for 30 minutes.

c) Rinse with DI H_2O and air dry with N_2 gas

d) Place the slides on a convection oven (NO. 658, Thermo scientific, USA) for 5 minutes at 65℃

2.2.2 Photolithography

Small structures or features can be created on the slides by photolithography. Then, these structures are basis for generating electrodes after metal deposit process. Figure 4 shows a photolithography procedure used in this thesis. According to the procedure for the device that was invented and experimented in this thesis, the photoresist left after developing is the shape of circle which is the shape of the traps.

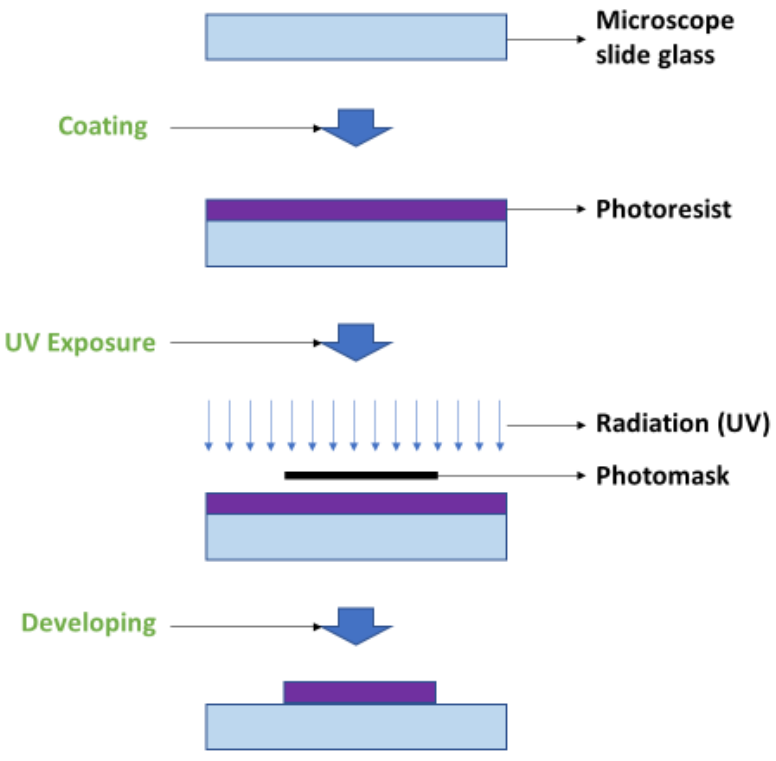

Figure 4. A schematic illustration of photolithography procedure using photoresist. The photolithography procedure consists of coating, UV exposure, and developing.

The detail procedures and used materials for photolithography is as follows:

1) Surface treatment
    a) Place a small petri dish at the bottom of a vacuum chamber with 8 ~ 9 drops of hexamethyldisilazane (HMDS) in it
    b) Place the slides on the rack of the vacuum chamber
    c) Vacuum for 5 minutes
    d) Stop vacuuming and close the valve and let it still for another 7 minutes
    e) Slowly ventilate the vacuum chamber
    f) Place the slides on a convection oven for 5 minutes at 65℃
2) Photoresist coating
    a) Place the slide on a vacuum spin coater (SCS 6800 Spin Coater, SCS, USA / Figure 5)
    b) Drop photoresist (AZ 5214E-IR Photoresist, IMM, USA) until it covers more than 80 % of the surface of the slide.
    c) Place the lid on the vacuum spin coater
    d) Set the spin coater parameters to 500 rpm, 15 seconds for the first step, and 2000 rpm, 30 seconds for the second step in one recipe
    e) Starting coating
    f) Place the slide on a hotplate for 70 ~ 90 seconds at 110 ℃

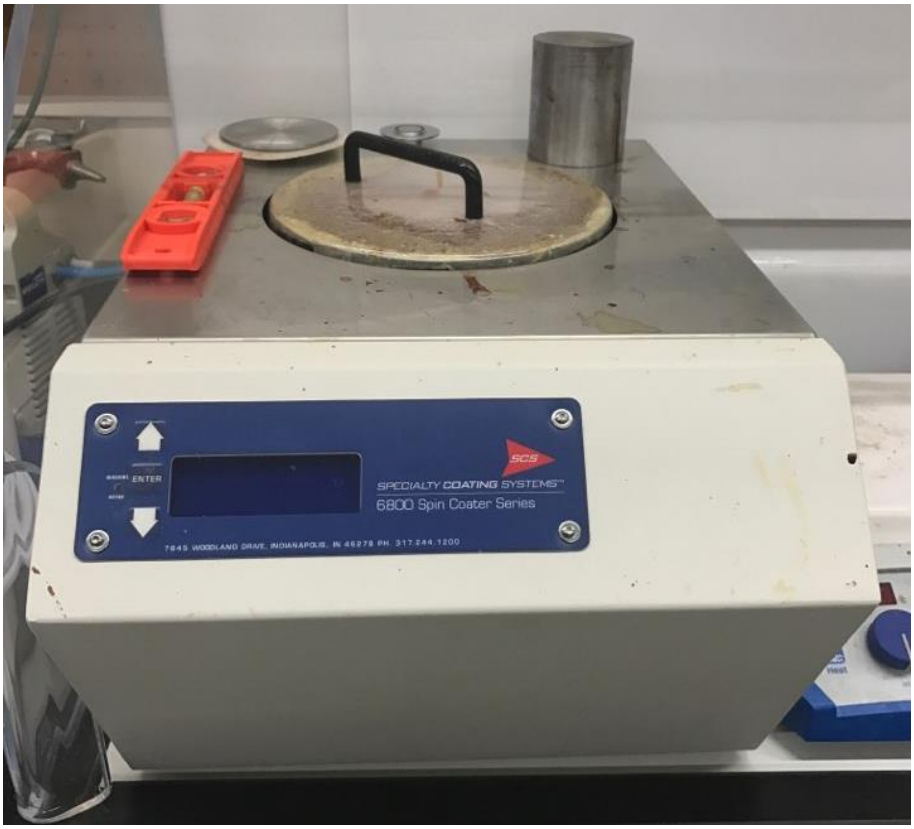

Figure 5. A vacuum spin coater

3) UV exposure

   a) Start a UV mask aligner (PLA-501-FA, Canon, Japan / Figure 6)

   b) Check gauges of vacuum, air, pressure and N_2

   c) Measure the intensity of UV with a UV intensity meter

   d) Rinse a photomask with DI H_2O and air dry with N_2 gas

   e) Place the photomask on the UV mask aligner

   f) Palace the slide under the photomask

   g) Expose UV light for 14 seconds at the UV light intensity of 7 mw/cm^2

      * The exposed time can be adjusted depending on the intensity of UV light

h) Remove the slide from the UV mask aligner

4) Developing

a) Mix a developer solution (NO. GHSBBG7070, AZ Electronic Materials, USA) with DI H_2O at the ratio of 1:4

b) Soak and stir the slide for 55 ~ 65 seconds

* The stirring time can be adjusted depending on a room temperature

c) Rinse the slide with DI H_2O for more than 30 seconds and air dry with N_2 gas

d) Bake the slide on a convection oven for 5 minutes at 65℃

Figure 6. A UV mask aligner

2.2.3 Metal deposit and lift-off

Metal deposit contribute to generating electrodes based on small structures or features that are created by photolithography. Figure 7 shows a schematic illustration of metal deposit and lift-off procedure after photolithography process. The invented devise in this thesis has hollow circular traps. It also states that the rest of circle shapes are electrodes deposited with chrome metal piece of purity 99% . Metal is deposited on the whole area of the slides first, then the photoresist with metal on it is peeled off from the slides in the process of lift-off, which remains the shape of electrodes.

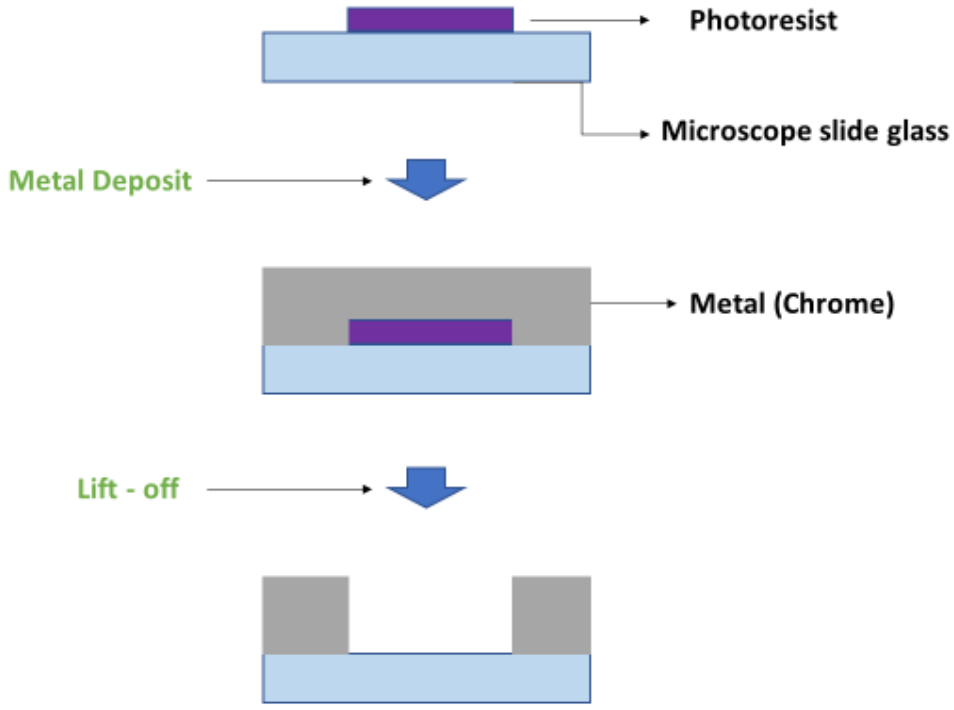

Figure 7. A schematic illustration of metal deposit and lift-off procedure. In this process, chrome was used as metal and acetone was used for lift-off.

The detail procedures and used materials from preparation to cleaning is as follows:

1) Metal deposit

a) Stick the slides treated by photolithography on a wafer using kapton tape

b) Place the wafer at the top of a chamber of a thermal evaporator (NO.KV-301-32987-B, Key high vacuum products, USA / Figure 8)

c) Place high purity chrome metal pieces inside a basket

d) Lay the basket inside the chamber and close a shutter

*Check the filament that the basket is connected

e) Apply vacuum grease around the rim of the chamber

f) Close the chamber and start the thermal evaporator

g) Check if a filament tap switch indicates the filament number the basket is connected

h) Turn off vent valve, foreline valve and high vacuum valve

i) Turn on roughing valve

j) Inject liquid nitrogen

k) Turn on mechanical pump for one hour

l) Turn on diffusion pump for two hours

m) Turn off roughing valve

n) Turn on foreline valve and high vacuum valve

o) Connect a crystal coolant tube

p) Set a program

* Density: 7.2, Z-Factor: 0.31

q) Turn on evaporation power supply and open the shutter

r) Control evaporation power to around 30

s) Control Ac ampere to around 150

t) Check and maintain the rate of deposit to 0.1 ~ 0.3 $\dot{A}$/s

u) Deposit until 1000 $\dot{A}$ at the rate of 0.1 ~ 0.3 $\dot{A}$/s and close the shutter

v) Turn off power control and power supply

w) Turn off diffusion pump and mechanical pump

x) Turn off high vacuum valve high vacuum valve

y) Turn on roughing valve and vent valve

z) Take off the slides and cool in a room temperature

Figure 8. A thermal evaporator

2) Lift-off

a) Place the deposited slides on a petri dish

b) Soak in acetone

c) Sonicate for 30 seconds

d) Rinse the slides with acetone

e) Check the shape of the electrodes with a microscope

* If photoresist in not washed off, repeat the process from b) to d)

f) Rinse the slides with DI H_2O and air dry with N_2 gas before use

2.3 Experimental setup

A variety of Lab-on-a-Chip (LOC) devices have been developed and used in different engineering areas during the past twenty years due to its advantages such as power efficiency, low contamination risk and reduced requirement for sample preparation [39, 40]. It has been contributing to the developments of microfabrication techniques. Since the first use of DEP in an LOC device [41], LOC became one of the main methods for DEP to be developed and applicated.

In this thesis, the fabricated DEP traps on a glass slide according to the process mentioned above were developed into LOC device with an indium tin oxide (ITO) glass slide, extra thin double-sided tape for spacer, and copper conductive adhesive tape. Then, this LOC device of electrical DEP traps were connected to a function generator, a microscope, and computers for a completed setup for manipulating particles.

2.3.1 Lab-on-a-Chip device with electrical DEP traps

The proposed LOC device consists of three layers as shown in Figure 9. The ITO layer (NO. IT10-111-25, NANOCS, USA) is one of the important components that functions as the

counter electrode. To maximize the benefit of transparent DEP traps, the transparent ITO layer was used, which enables to observe and monitor movements of particles inside the traps.

A spacer (Nitto Denko Co, Japan) that secures the area for DEP force effect was embedded between the ITO layer and the chrome microelectrode on the microscope slide glass. The spacer plays an important role by maintaining the gap between ITO electrode and chrome microelectrodes, which results in stable and constant particles' flow inside the microchannel. The spacer was tested many times and no fluid leakage was found.

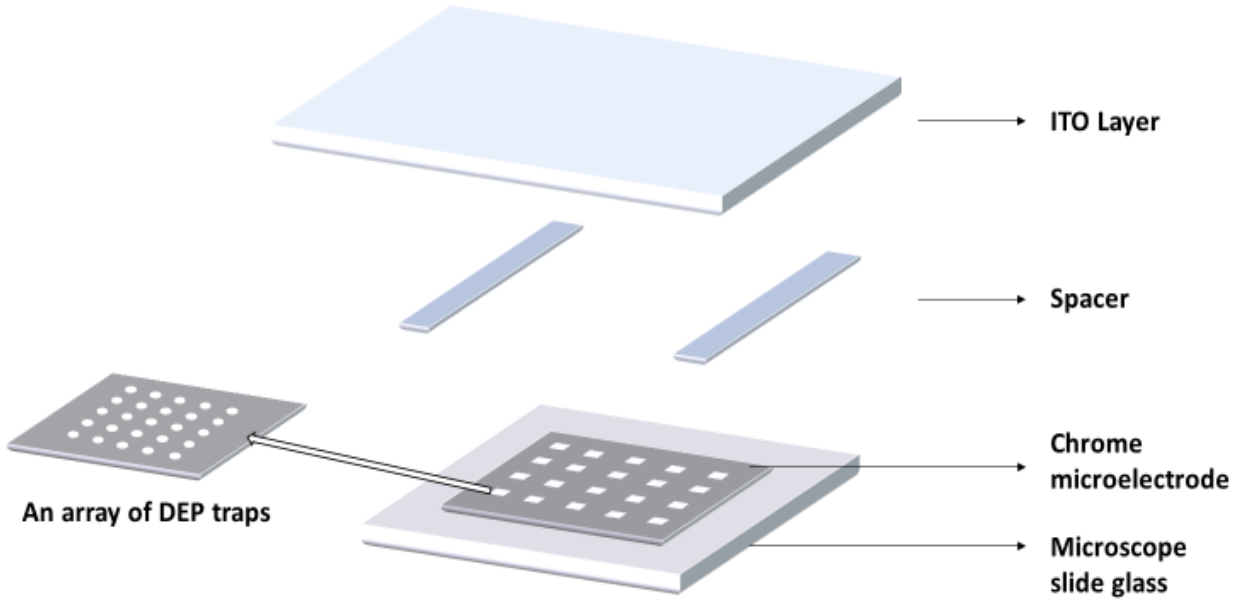

Figure 9. A schematic diagram of the LOC device with electrical DEP traps. The coated ITO glass and chrome function as electrode. The spacer provides the gap between ITO electrode and chrome microelectrodes ensuring constant particles' flow inside the microchannel.

Several groups of an array of DEP traps were fabricated on the chrome microelectrode as shown in Figure 10. Each square shaped array consists of 80 ~ 100 same sized circular DEP traps. From 10 μm to 40 μm circular DEP traps were fabricated with from 10 μm to 50 μm gap between each circular DEP trap to compare the difference depending on the size of DEP traps. In this thesis, from 10 μm to 40 μm circual traps with 20 μm gap and 40 μm circular traps with 40 μm gap were used.

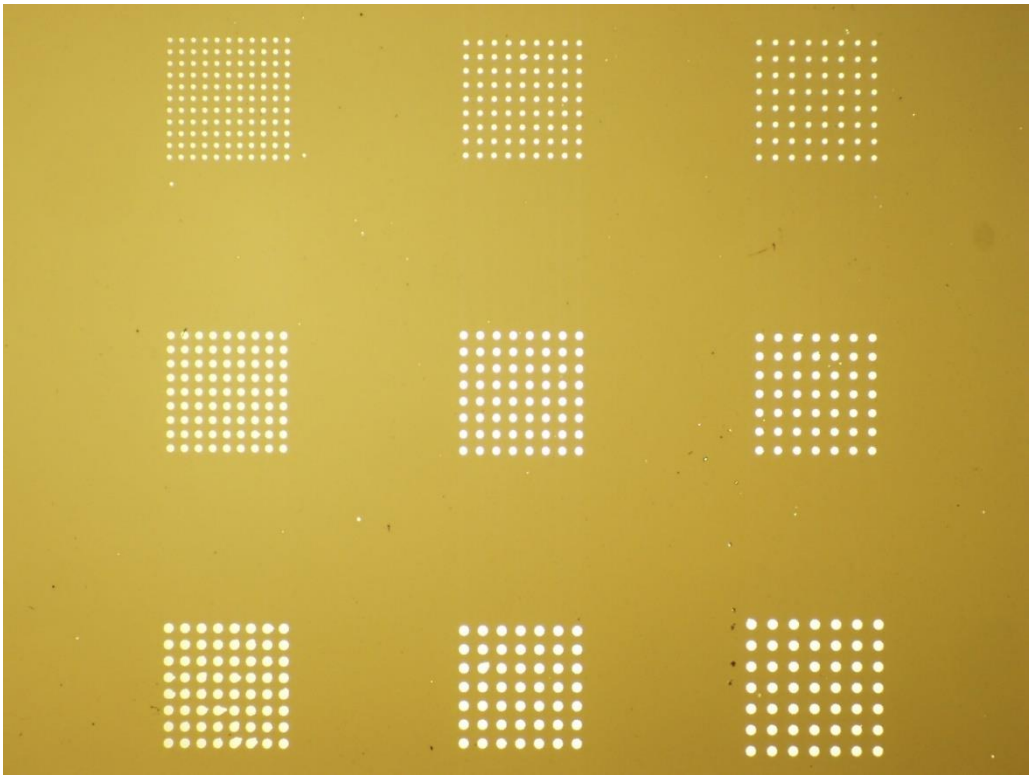

Figure 10. Arrays of DEP traps with different sizes of traps and gaps. The first column consists of 20 μm*, 30* μm*, 40* μm *circular DEP traps with 20* μm *gap from the top. The second column is 30* μm *gap and the last column is 40* μm *gap with the 20 ~ 40* μm *DEP traps.*

Material and dimension of each component in the LOC device are described in Table 2. The ITO coated glass was cut longer than the bottom glass to connect to a copper conductive adhesive tape that also functions as a counter electrode. In the thesis, 30 μm spacer was used to verify the difference of the DEP force field depending on the thickness of the spacer.

Component	Material	Dimension		
		Length	Width	Thickness
ITO Layer	Indium tin oxide	35.4 mm	25.4 mm	1 mm
Spacer	Polyester	20.5 mm	2.5 mm	30 μm
Chrome Microelectrode	Chrome	18.0 mm	18.0 mm	100 nm
Microscope Slide Glass	Glass	25.4 mm	25.4 mm	1 mm

Table 2. Specifications of each component of the proposed LOC device with the electrical DEP traps. One side of the ITO coated slide glass is longer than the bottom sidle glass to be used as a ground electrode.

2.3.2 Electrical DEP trap setup

The ITO electrodes and chrome microelectrodes of the LOC device with the circular DEP traps were to the function generator (NO. 33220A, Agilent Technologies, USA) through flexible wires. Then, the LOC device was placed on the microscope (NO. BX53, Olympus, Japan) with two cameras for observation and digital image acquisition respectively. The microscope was connected to two cameras as shown in Figure 11; one is equipped in the microscope for live time

observation, and the other one is the high-speed camera for accurate analysis of particles' movements.

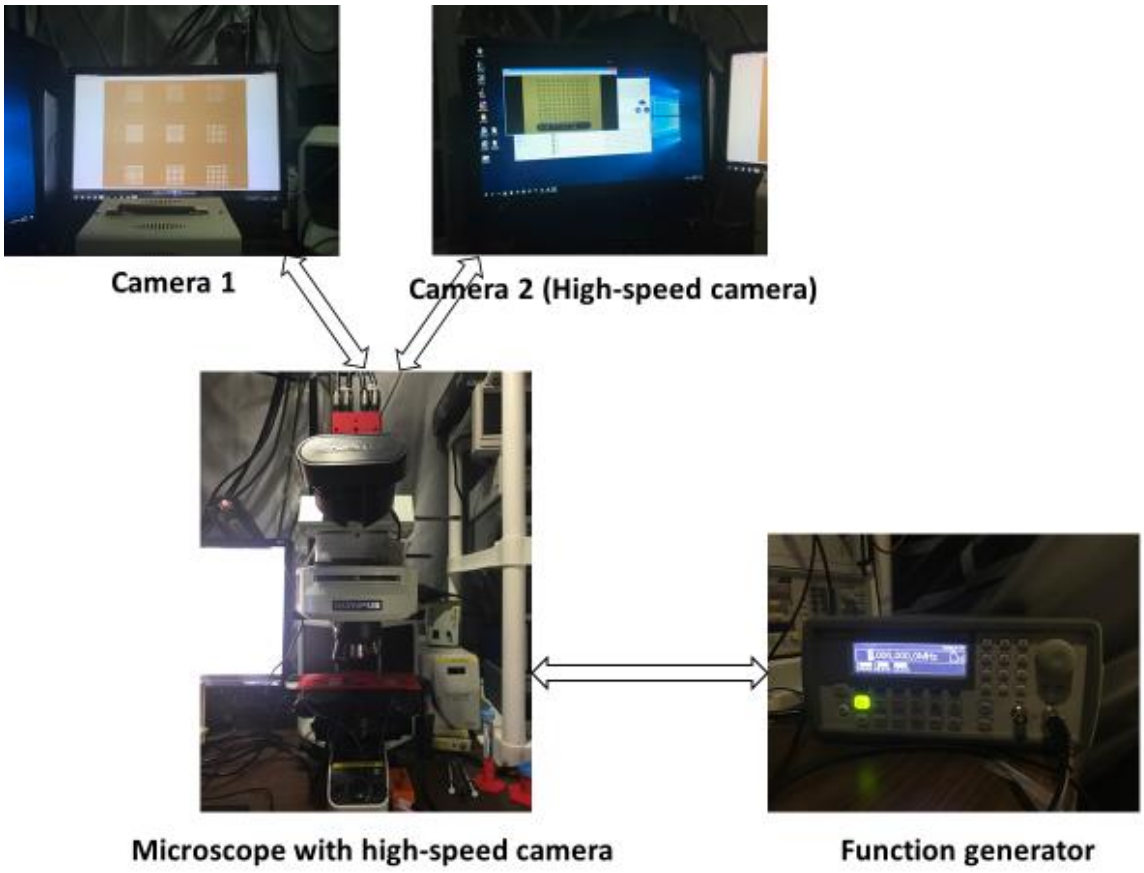

Figure 11. The experimental setup for capturing single particles and measuring its movements on the array of circular DEP traps.

The function generator was used to control applied frequencies and voltages to the DEP trap system. Positive and negative DEP depends on the applied AC electric field. In this thesis, 1 MHz frequency was mostly used to induce negative DEP force to particles, which move particles towards the center of the circular DEP traps where the electric field gradient is low.

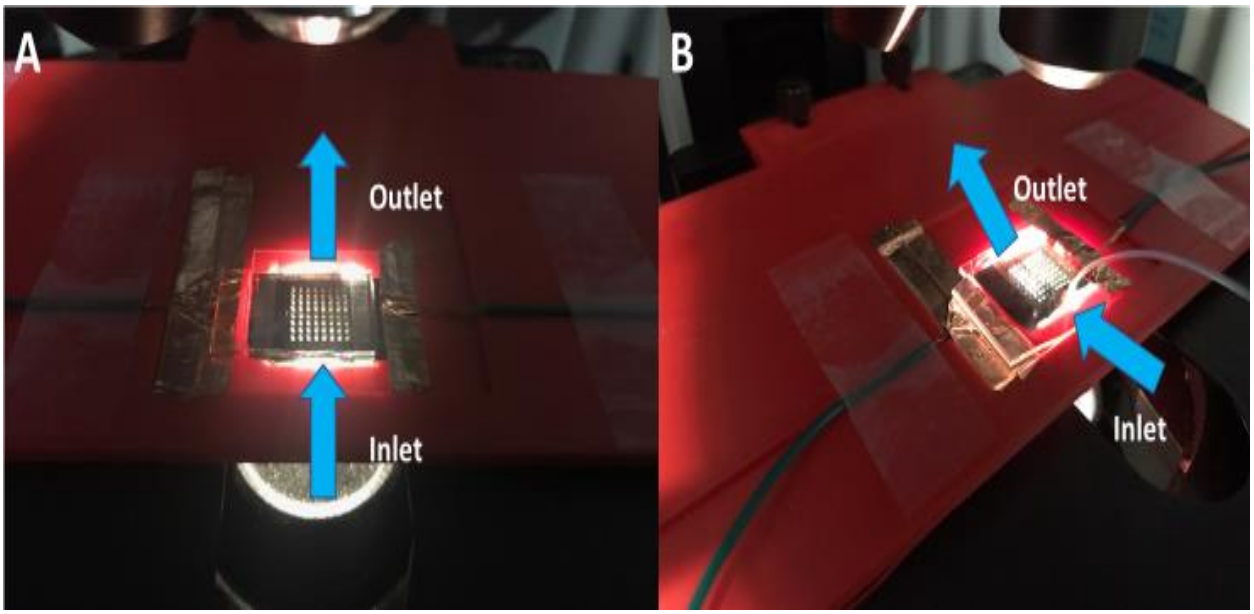

Figure 12. The inlet and outlet of the suggested LOC device: (A) using osmotic pressure; (B) using syringe pump

Figure 13. A syringe pump

To control the flow of particles, both osmotic pressure and syringe pump were used. The inlet and outlet were located each side of the DEP traps that were not blocked by the spacers as

shown in Figure 12. Even though both methods were used, the inlet and outlet locations were directed to the same way. Especially, the syringe pump (KDS 200, KD scientific, USA) in Figure 13 was used for particle separation experiments in this thesis due to the advantage of maintaining the same pressure.

2.3.3 Digital image acquisition

The high-speed camera (CL-400, Allied Vision, USA) was used to measure exact movements and velocities of each single particle with the digital image acquisition program (XCAP™ Image Processing Software, EPIX Inc). In this thesis, each particle's velocity was measured based on the travel distance of a single particle and the travel time. Travel distance was obtained by two consecutive pictures using the image processing program (Image J, National Institutes of Health) and travel time was acquired based on the frame duration. The mode was set up as shown in Figure 14. Most importantly, the frame duration was set up and controlled from 10 frames / second to 50 frames / second depending on the particles' velocity.

Figure 14. The mode setup of the digital image acquisition program (XCAP™ Image Processing Software, EPIX Inc). The setups were consistent throughout the experiments except for Frame duration and Exposure which were controlled depending on the particles' velocity.

2.4 Numerical simulation of DEP trap

Dielectrophoresis has been studied numerically using commercial FEM software to analyze electrical fields and dielectrophoretic forces. Especially, COMSOL Multiphysics which is one of the well-established commercial FEM software have been used in many studies for analyzing Dielectrophoresis [42, 43].

In this thesis, each experimental operation condition was generated by finite element method (FEM) using computer software (COMSOL Multiphysics V5.2, COMSOL Inc) as shown in Figure 15 to evaluate a particle's physical properties at the single particle level. Governing equations were analyzed and interconverted to conduct desired simulations in COMSOL. Physical and boundary conditions were also considered and tested to match the results of simulation to general traits of DEP trap.

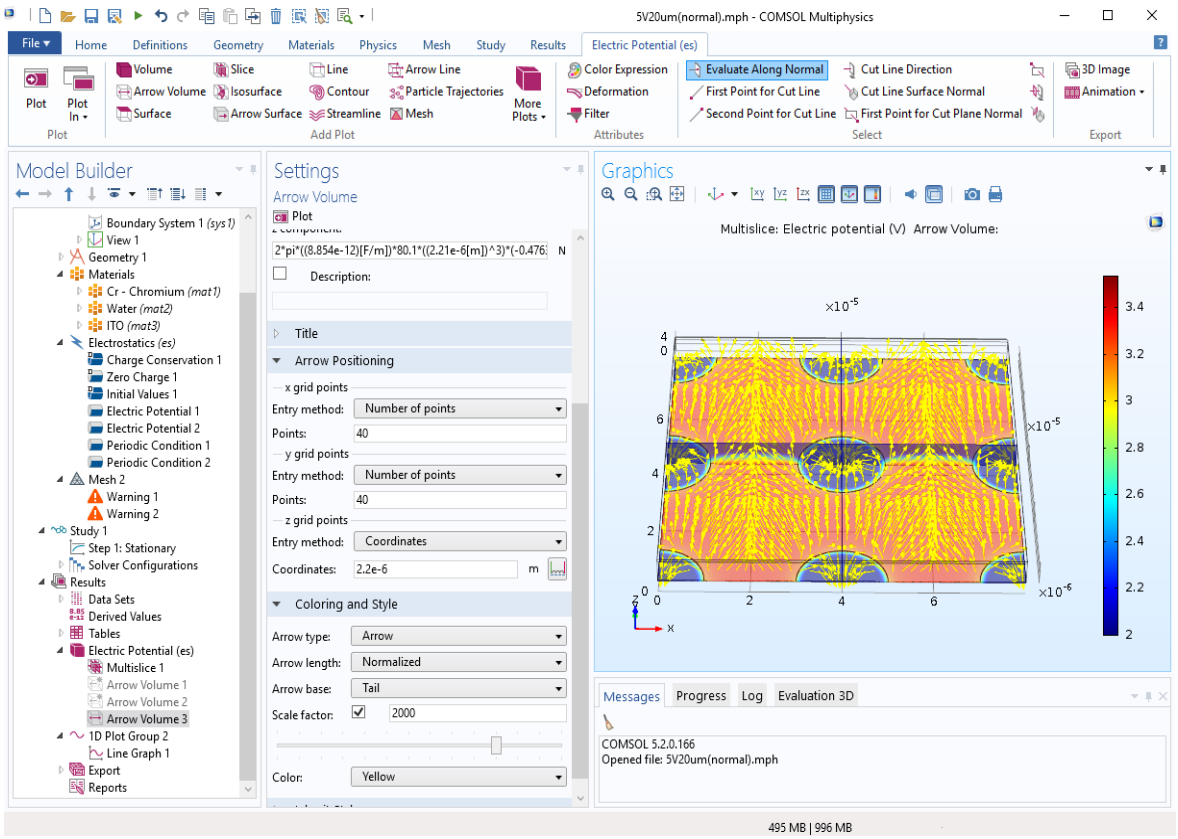

Figure 15. The finite element analysis, solver, and simulation software, COMSOL Multiphysics V5.2.

Direction and magnitude of the force field inside and outside circular traps were analyzed to find the optimum condition for single particle trapping. The movement of a particle in both outside and inside a trap was predicted based on the simulated force field. The magnitude of DEP force applied on a 4 μm polystyrene particle was ranged from 0 to 0.285 nN when from 0 to 8 V was applied. The particles that have identical physical and electrical properties can be simultaneously separated from the mixture using a developed method.

2.4.1 Physics and governing equations

Proper physics and governing equations are the most important factors to analysis a system numerically. In this thesis, 3D space demention was selected to simulate length, width, and depth of the LOC device. Then, the electrostatics interface was used to compute the electric field which causes the DEP force field with polarized particles. In COMSOL software, the physics interface solves Gauss' Law for the electric field using the scalar electric potential as the dependent variable.

To derive a DEP force which exerts on a particle in non-uniform electric field, the governing DEP Equation 1 was transformed as follows for x component:

$$2 * \mathrm{pi} * ((\varepsilon_o)[\mathrm{F/m}]) * \varepsilon_m * ((\mathrm{r[m]})\hat{}3) * \mathrm{Re[K}(\omega)] * (2 * \mathrm{es.Ex} * \mathrm{d(es.Ex, x)} + 2 * \mathrm{es.Ey} * \mathrm{d(es.Ey, x)} + 2 * \mathrm{es.Ez} * \mathrm{d(es.Ez, x)}) \quad (4)$$

Especially, the electric field gradient, ∇E^2, in Equation 1 was properly modified in Equation 4 for compatibility with the computer software. Equation 2 and 3 were also transformed as follows for y and z components to enable those governing equations to be applied in the COMSOL software.

$$2 * \mathrm{pi} * ((\varepsilon_o)[\mathrm{F/m}]) * \varepsilon_m * ((\mathrm{r[m]})\hat{}3) * \mathrm{Re[K}(\omega)] * (2 * \mathrm{es.Ex} * \mathrm{d(es.Ex, y)} + 2 * \mathrm{es.Ey} * \mathrm{d(es.Ey, y)} + 2 * \mathrm{es.Ez} * \mathrm{d(es.Ez, y)}) \quad (5)$$

$$2 * \mathrm{pi} * ((\varepsilon_o)[\mathrm{F/m}]) * \varepsilon_m * ((\mathrm{r[m]})\hat{}3) * \mathrm{Re[K}(\omega)] * (2 * \mathrm{es.Ex} * \mathrm{d(es.Ex, z)} + 2 * \mathrm{es.Ey} * \mathrm{d(es.Ey, z)} + 2 * \mathrm{es.Ez} * \mathrm{d(es.Ez, z)}) \quad (6)$$

The value of the permittivity of the free space, ε_o, and the relative permittivity of the surrounding medium, ε_m, which is DI water in this case were used from an earlier paper [44] using the value 8.854^{-12} and 80.1 respectively. The real part of the Clausius-Mossotti factor, $Re[K(\omega)]$, was also derived from the earlier paper [44] that has been studied by a co-worker in the Dr. Chang's lab. The real part of the Clausius-Mossotti factor was – 0.4763 on the condition of polystyrene bead, 1 MHz applied frequency, and 2 ~ 4 $\mu S/cm$ conductivity, which was the same condition in the experiments for this thesis.

2.4.2 Geometry and boundary conditions

The simplest geometry is required in most numerical methods to get proper and concise simulation results by avoiding unnecessary errors which may occur due to its complex geometry. Periodic conditions were applied in this numerical analysis by taking the advantage of the DEP traps' repeated circular shapes. The application of periodic conditions was beneficial for avoiding unnecessary computation and guaranteed less effort for the simulation.

To simulate the array of the circular DEP traps as shown in Figure 3, one circular DEP trap was designed at the center of the geometry. Then, eight half circular DEP traps were designed around the center circular trap as shown in Figure 16.

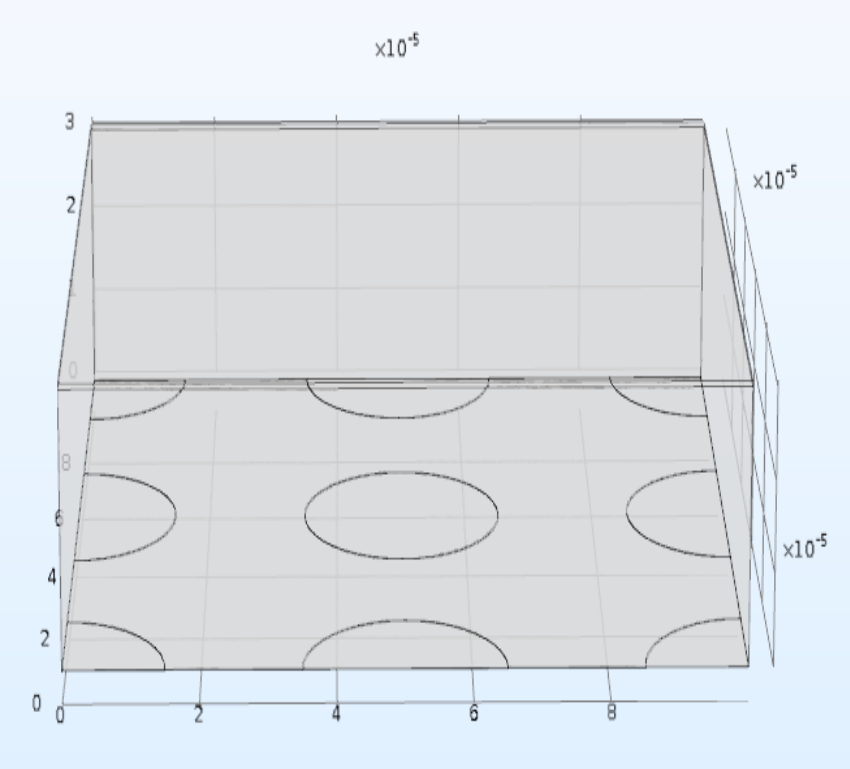

Figure 16. Geometry of the suggested LOC device with the circular DEP traps. The device has 20 μm DEP traps with 20 μm gap between each trap. Periodic condition was applied to every side of the device to express its continuity.

The depth of the first bottom block was 100 nm that was the same depth as the deposited chrome metal on the bottom microscope slide glass. The depth of the second block above the bottom block was 30 μm as the depth of the spacers. The third and top block of the LOC device was 600 nm which is the depth of coated ITO on the slide glass. The circular DEP trap sizes and the gap between two DEP traps varied according to the sizes of the array. The overall simulation parameters for the one of the most used geometries in this thesis is as shown Table 3.

Simulation geometry	Actual materials	Dimension		
		Length	Width	Thickness
Bottom layer	Chrome	80 μm	80 μm	100 nm
Middle layer	Medium (DI water)	80 μm	80 μm	30 μm
Top layer	ITO	80 μm	80 μm	600 nm
Trap circle	None	20 μm	20 μm	0 nm
Gap	Chrome	20 μm		100 μm

Table 3. Simulation parameters for the array of the 20 μm circular DEP traps with 20 μm gap. Thickness parameters were set consistently throughout the experiments, while length and width varied according to the trap size and gap. Thickness of trap is 0 because the trap itself is hollow and the surrounding area was deposited with 100 nm depth chrome metal.

2.4.3 Materials

Three materials were used in simulating the LOC device; chromium, water, and ITO. Applied values of each material's properties for the simulation were based on the default material properties in COMSOL Multiphysics except for relative permittivity. Relative permittivity of chromium, water, and ITO are not loaded in COMSOL Multiphysics. These values were previously studied and cited from the published articles [44, 45]. The important property values of those materials are listed in Table 4.

Materials	Electrical conductivity	Relative permittivity
Chromium	7.9×10^6 S/m	12
Water	5.5×10^{-6} S/m	80.1
ITO	1.3×10^6 S/m	3.3378

Table 4. Electrical properties of materials for the LOC device. Electrical conductivity is one of the main factors that is involved in generating electric field. For a given electric field, a material with high conductivity produces more current flow. Relative permittivity was used to calculate electric displacement field.

Electric displacement field, D, means the influences of an electric field, E, to the organization of electric charges in a given medium in conjunction with charge migration and electric dipole reorientation. The relationship between an electric displacement field and an electric field is as follows;

$$\mathrm{D} = \varepsilon_0 \varepsilon_r E \tag{7}$$

where ε_o is the permittivity of free space, ε_r is the relative permittivity. Equation 7 was applied in the Electrostatic section in the simulation. The values of the relative permittivity were used from the material properties and the value of 8.854×10^{-12} was used for ε_o, which is the ratio $\frac{D}{E}$ in free space.

2.4.4 Mesh

Mesh is important in obtaining reliable numerical simulation results. In most cases, the finer the mesh is, the more exact data can be achieved. In this thesis, a physics-controlled mesh was used for the experiments with 30 μm spacer.

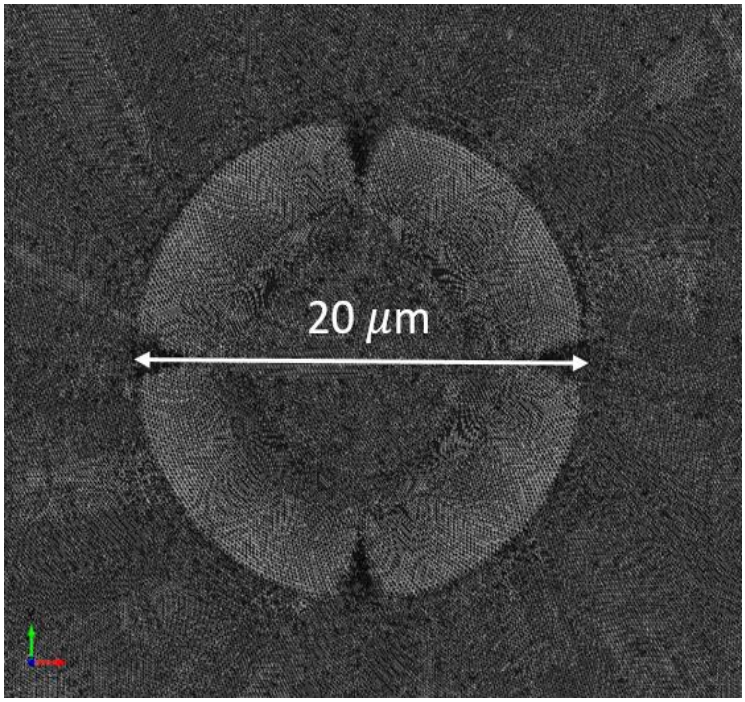

Figure 17. Mesh of the array of 20 μm DEP traps with 30 μm spacer.

The array of DEP traps with 30 μm spacer was meshed using a physics-controlled mesh with the finest element size among the options, which is Extremely fine as shown in Figure 17. Even though it was simulated under the finest mesh option, some element size was bigger than 0.2 μm, which was proved to be reliable for a micro scale observation [44]. It was due to its enormous volume and the limited performance of the simulation computer. However, the analyzed area for acquisition of data -around and inside the circular traps- was mostly smaller than 0.2 μm in size.

To enhance the accuracy of the analysis of the simulation, each derived graph's resolution was adjusted from Normal resolution to Extra fine resolution, which led into shorter girds between each date value in the graphs. In addition to that, whole obtained data sets from

the simulations were interpolated up to 0.01 μm accuracy to differentiate a particle's traveled distance inside the DEP traps.

Chapter 3

DEP Force Simulation

3.1 Overview

Each case of experiment in this thesis was numerically simulated to confirm the location and force of the captured microparticle inside the trap based on the direction and amplitude of the DEP force field. The extracted data from the simulation was also used to explain the unique properties of the DEP traps.

The graphics of the DEP force field was acquired as a part of analysis to visualize the directivity and the relative magnitude of the DEP force. Secondly, the applied DEP force on a particle was extracted and made into a line graph to quantify the exact force strength. To simulate force field and make a line graph of force, particles were assumed to be close enough to the bottom of the LOC device and the force applied on those particles were extracted based on particle's radius. According to simulation, particles' proximity to the bottom of the device affects the strength of the DEP force; the closer particles are to the chrome electrodes, the more strength they have.

In this section, two main results from the simulation are introduced with explanations, and differences of the DEP force based on applied voltages are illustrated. The differences of the DEP force based on a size of particle, a size of DEP trap, and a thickness of spacer were also analyzed and those results are discussed in the next chapter in conjunction with experimental methods.

3.2 DEP force data analysis

The DEP force field in this simulation represents both the directivity and relative magnitude of the DEP force which enable to predict the detailed properties of the DEP traps before actual experiments. Based on the graphical results from the simulation as shown in Figure 18, there are two significant characteristics of the suggested circular DEP traps that facilitate capturing a particle at a required position and capturing a particle selectively depending on a speed or force of a particle. Polystyrene beads (Spherotech, USA) were used as particles throughout the both experimental and numerical analyses in this thesis.

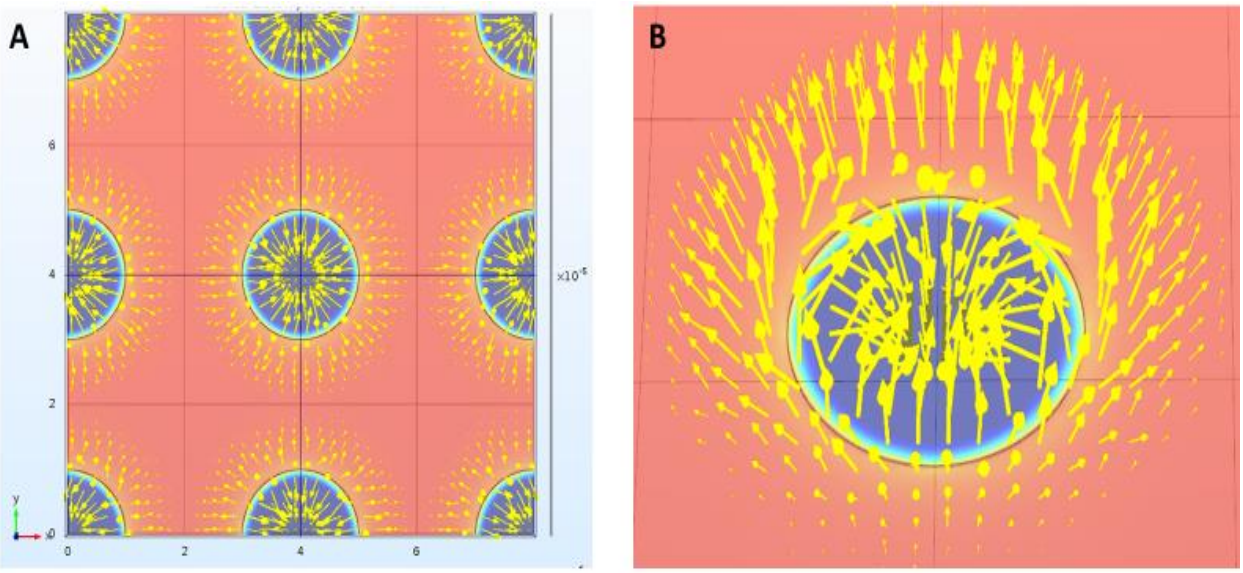

Figure 18. The graphical results of circular DEP traps from the numerical computer simulation: (A) the DEP forces inside the trap exert toward the center of trap; (B) the strongest forces are generated at the rim of trap and the repulsive forces are observed outside the rim. It is also discovered that Z-axis force exists as well as X-axis and Y-axis forces.

First of all, it is observed that the DEP forces on a particle converge at the center of the DEP trap as shown in Figure 18A. This convergence of the DEP force field is the main property of this trap that facilitates capturing a particle under negative DEP force. Each arrow represents

the negative DEP force that affect a particle when a particle is located at the same position as the arrow. Arrow length was set logarithmic so that the length of each arrow could also represent a relative strength of DEP force. Every circular trap shows the same force field due to its omnidirectional and symmetric characteristics.

Secondly, it can be predictable that the strongest forces are generated at the rim of trap considering the length of arrows in Figure 18B. In addition to that, the repulsive forces are observed outside the rim which can be used to capture a particle selectively depending on a speed or force of a particle. Z-axis force is also observed as X-axis and Y-axis forces. Z-axis forces pointing upward are mostly around and outside the rim and Z-axis pointing downward and the center of the trap are observed inside the trap. This trait plays an important role in this thesis and the detailed explanations will be discussed at the next chapter in conjunction with the experimental results.

The negative DEP force field on the graphical results in Figure 18 was extracted and converted into a line graph to quantify the exact force strength which helps analyze the properties of the traps more thoroughly. The DEP force strength of each axis is as shown in Figure 19. Since a particle was approaching and trapped along the extended line that penetrates the center of the trap in all experiments, Y-axis force component was negligible compared to X-axis and Z-axis force components.

In case of X-axis force, negative value represents the X-axis force that exerts towards left direction, while positive value represents the X-axis force that exerts towards right direction. As expected from Figure 18, X-axis forces is repulsive outside the circular trap and converged at the center inside the trap. This characteristic of repulsive force enables to separate different sizes'

particles by repelling particles that are under stronger DEP force due to its size. The strongest X-axis force is generated at the right inside of the rim as 2.5×10^{-10} N. The reason that the strongest force doesn't take place at the rim is because the location that was used to derive the graph is particle's radius. If the graph is simulated at the location of the bottom, the strongest force is generated at the exact location of the rim.

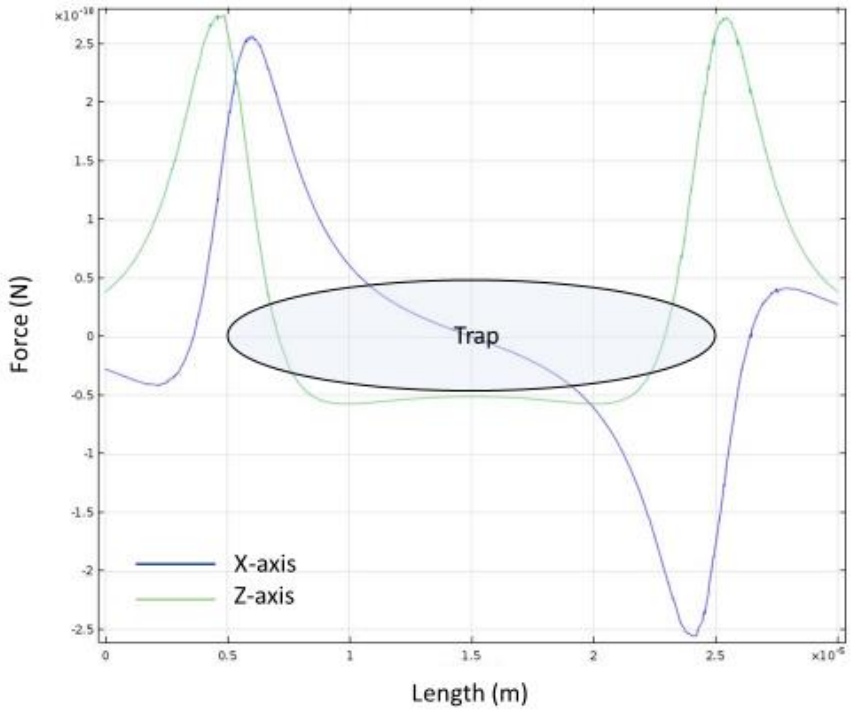

Figure 19. X-axis and Z-axis force field line graph. In case of X-axis force, positive force represents the force exerting towards left as opposed to negative force that represents the force exerting towards right. In case of Z-axis force, positive force represents the force exerting upward as opposed to negative force that represents the force exerting downward.

In case of Z-axis force, negative value represents the Z-axis force that exerts downward, while positive value represents the Z-axis force that exerts upward. It is noteworthy that Z-axis

forces are almost the strongest around the rim and towards upside. The reason the strongest force is not generated at the rim is the same as the strongest X-axis forces. In the opposite, Z-axis forces are less strong inside the trap and towards downside. This Z-axis downward force facilitates trapping a particle inside a trap by seizing a particle at the bottom of the trap.

3.3 DEP force with different applied voltages

The graphics of the DEP force field and its line graphs are one of the most important factors to comprehend the effect of the DEP traps and quantify particle's physical properties. The numerical simulation was conducted changing trap sizes, particle sizes, applied voltages and even spacer sizes to fully understand the characteristics of the suggested DEP traps. In this section, the computer simulation results about the DEP force field depending on the applied voltages from 5 V to 8 V are demonstrated. The other numerical simulation results such as different particle sizes, trap sizes and spacer sizes are analyzed in conjunction with the experimental methods in the next chapter.

The graphic results of the DEP force field were generated changing the applied voltage from 5 V to 8 V to demonstrate the differences depending on the applied voltages. In all cases including this case, the applied frequency was set as 1 MHz because the applied frequency determines whether the system can be under negative DEP or positive DEP. It is not related to the strength of DEP force field. Besides the voltages and frequency, 20 μm trap with 20 μm gap between the traps were simulated. The depth of spacer was set as 30 μm.

The DEP force field increased as the applied voltages increased as shown in Figure 20. The direction of each arrow represents the direction of negative DEP force that exerted on a

particle at the same location of an arrow and the length of each arrow represents the strength of negative DEP force on a particle. The scale factor of arrow in the pictures was set as the same value to be compared objectively. The length of arrow gets longer as the applied voltage increases up to 8 V. It can be predictable that a higher voltage is more efficient in capturing and trapping a particle inside the trap.

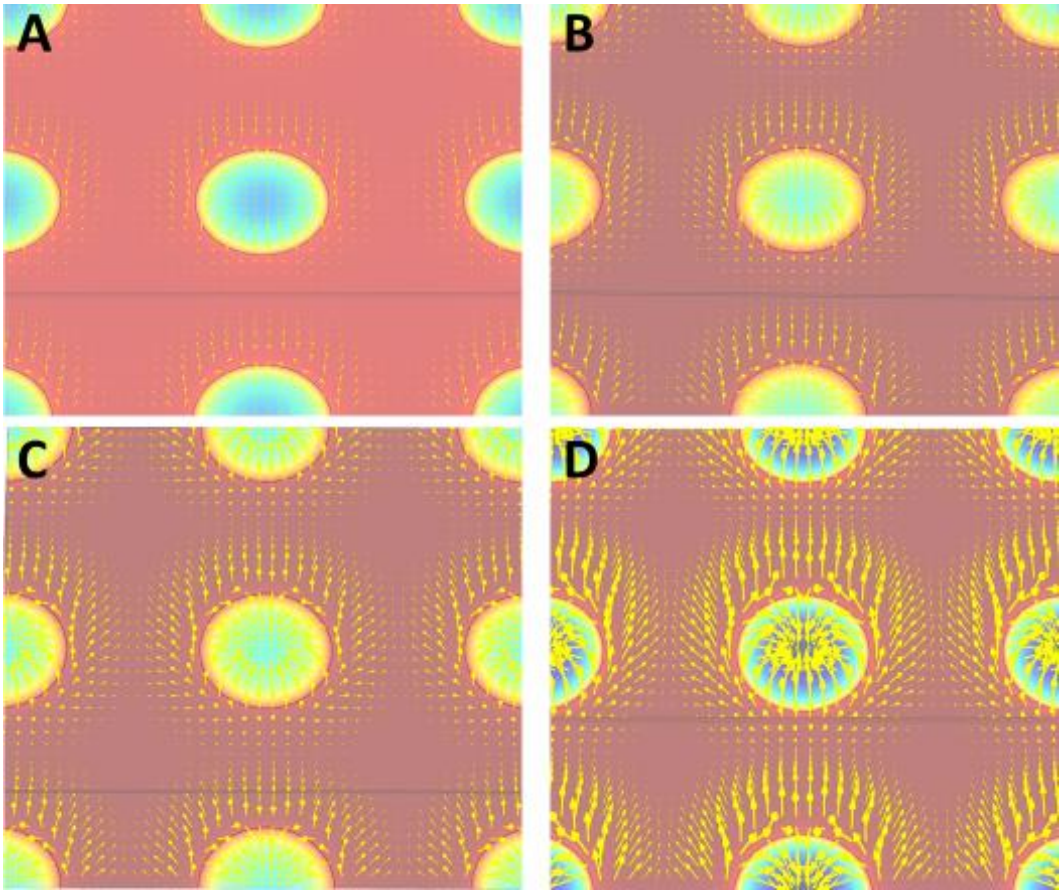

Figure 20. Direction and strength of negative DEP force that exerts on a particle depending on the applied voltage: (A) 5 V; (B)6 V; (C) 7 V; (D) 8V. The strength of DEP force increases as the applied voltage increases, while the direction of DEP remains the same.

The direction and strength of negative DEP force in Figure 20 were converted to a line graph as shown in Figure 21. Each graph shows the exact values of DEP force in X-axis and Z-axis. In accordance with the graphic results of the DEP force field, it is confirmed that the higher voltage was applied, the stronger DEP force field was generated. In particular, it is notable that the strongest X-axis force of the trap where 8 V was applied to is 4.56×10^{-10} N and the strongest X-axis force of the trap with 5 V is 1.78×10^{-10} N. The trap with 8 V is 2.56 times stronger than the trap with 5 V. The difference of Z-axis force between 5 V and 8 V can be measured in the same way and their difference is 2.96×10^{-10} N in positive values and 5.45×10^{-11} N in negative value.

The direction of DEP force can be analyzed by checking if the force has positive or negative value. As mentioned before, positive X-axis force represents the force exerting towards left as opposed to negative force that represents the force exerting towards right. In case of Z-axis force, positive force represents the force exerting upward as opposed to negative force that represents the force exerting downward.

By converting the graphic results of the DEP force field into the line graphs, numerical analysis became possible. Each force factor either in X-axis or Z-axis can be compared based on objective numerical data. This numerical method plays an important role in quantifying a particle's physical properties such as speed and moving force when it is conducted with experimental methods.

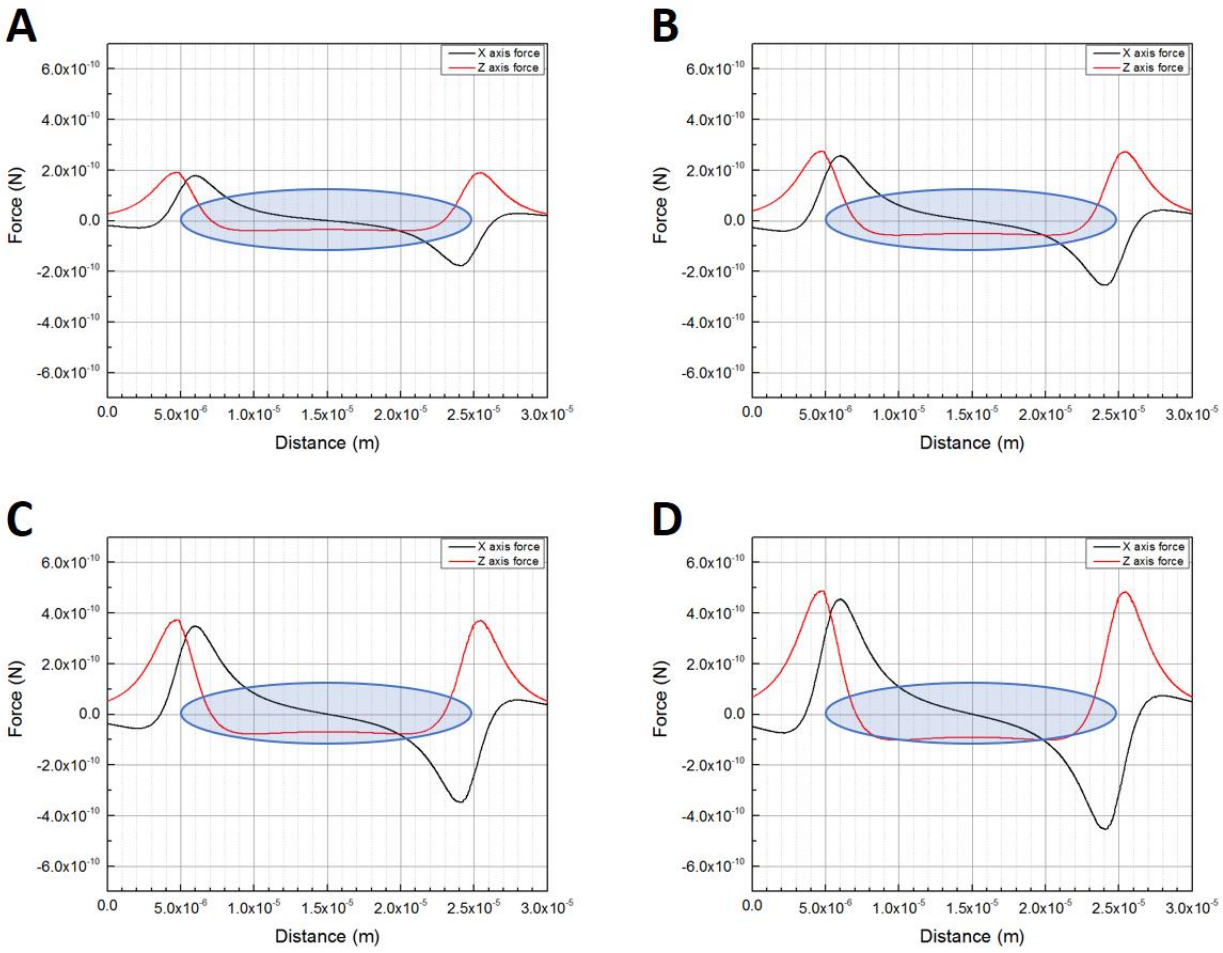

Figure 21. Line graphs of negative DEP force in X-axis and Z-axis that exerted on a particle depending on the applied voltage: (A) 5 V; (B)6 V; (C) 7 V; (D) 8V. The transparent circle represents the size of the trap. The forces in both X-axis and Z-axis increase as the applied voltage increases from 5 V to 8 V. It is notable that each objective force value can be measured and compared, which facilitates quantifying a particle's physical properties such as speed and moving force when it is conducted with experimental methods.

Chapter 4

Trapping Experiment

4.1 Overview

In this chapter, more complex experiments and analyses are presented than the previous chapter using both experimental and numerical methods. First, trapping beads with various sizes of traps such as 10 μm, 20 μm, 30 μm, 40 μm traps are demonstrated. A concept of work is introduced to compare each trap's efficiency in relation to particles' speed. Correlation between X-axis and Z-axis DEP force is thoroughly analyzed to illustrate the unique properties of the suggested DEP traps. In particular, diverse behaviors of a particle under the Z-axis force effect are diagramed and proved with the actual experimental pictures.

Secondly, trapping various sizes of beads from 2 μm to 10 μm under the same trap is presented. Due to X-axis repulsive force around the rim of the trap, the results of this experiment suggests the possibility of separation of various sizes' particles. Repulsive force at the rim that enables to separate different sizes' particles is analyzed to find an optimized trap for separation depending on particle's size. Experimental pictures are also presented to prove the actual repulsive force effect.

Lastly, separation of 4 μm and 6 μm particles from the mixture of 2 μm, 4 μm, and 6 μm particles is demonstrated. This separation technique requires thorough understanding of every property of the circular DEP traps such as the repulsive force and the Z-axis force effect. This work also suggests the application of the DEP trap as a microparticle's filter.

4.2 Trapping beads with various sizes of traps

Numerical method was first applied to analyze the general traits of the circular DEP traps depending on the trap size in prior to the experimental method and analysis. The same experimental conditions were applied throughout the whole experiment's procedures in this thesis. Particles were assumed to be close enough to the bottom of the LOC device and the yielded DEP force field represented the force that exerts on a particle when it moves along the bottom of the electrodes. In this case, the height of the center of a particle was considered as 2 μm because its diameter is 4 μm. The applied frequency was set as 1 MHz, which resulted in generating negative DEP in the LOC device. The 10 μm, 20 μm, 30 μm, and 40 μm traps with 20 μm gaps between the traps were simulated. The depth of spacer was set as 30 μm.

The acquired graphics of the DEP force field visualized the directivity and the relative magnitude of the DEP force as shown in Figure 22. Unlike the results of the previous experiment with different applied voltages, it was observed that each trap had its own characteristic depending on the trap size and the strength of DEP force didn't simply increase linearly in accordance with the trap size. Considering the length and directivity of the arrows in the result of simulation, the 10 μm trap had less powerful combined forces than other size traps. However, the strongest force that was generated at the rim reached to the center of the trap, which was predicted to be an important factor to capture a particle inside the trap. In the opposite, the repulsive force around the rim was barely observed. In the 20 μm trap, the overall combined DEP force was observed to be stronger than the 10 μm trap. The DEP force was still generated at the center of the trap. However, the strength of force at the center was not as strong as the 10 μm trap even though the strongest force at the rim was observed to be stronger than the 10 μm trap. The repulsive force was witnessed, but the strength was predicted to be still insignificant. The

difference between the 10 μm trap and the 20 μm trap had a similar tendency to the difference between the 20 μm trap and the 30 μm trap.

The strongest combined force at the rim was stronger in the 30 μm trap than the 20 μm trap. In addition, the repulsive force around the rim was also observed to be stronger in the 30 μm trap. However, the DEP force at the center in the 30 μm trap was not observed as effective as the 20 μm trap to capture and immobilize a particle at the center of the trap. It showed insignificant strengths compared to strengths of the forces at the rim. In case of the 40 μm trap, the strength of force at the rim was the highest. The repulsive force around the rim was also observed to be the strongest force among the 10 μm ~ 40 μm traps. Especially, this repulsive force was considered to be a significant amount of strength that could affect particles by repelling away from the trap. The DEP force at the center was simulated to have minor effect showing almost no force. It suggested that a captured particle could not be located at the center even though the trap has enough force to trap a particle inside the trap.

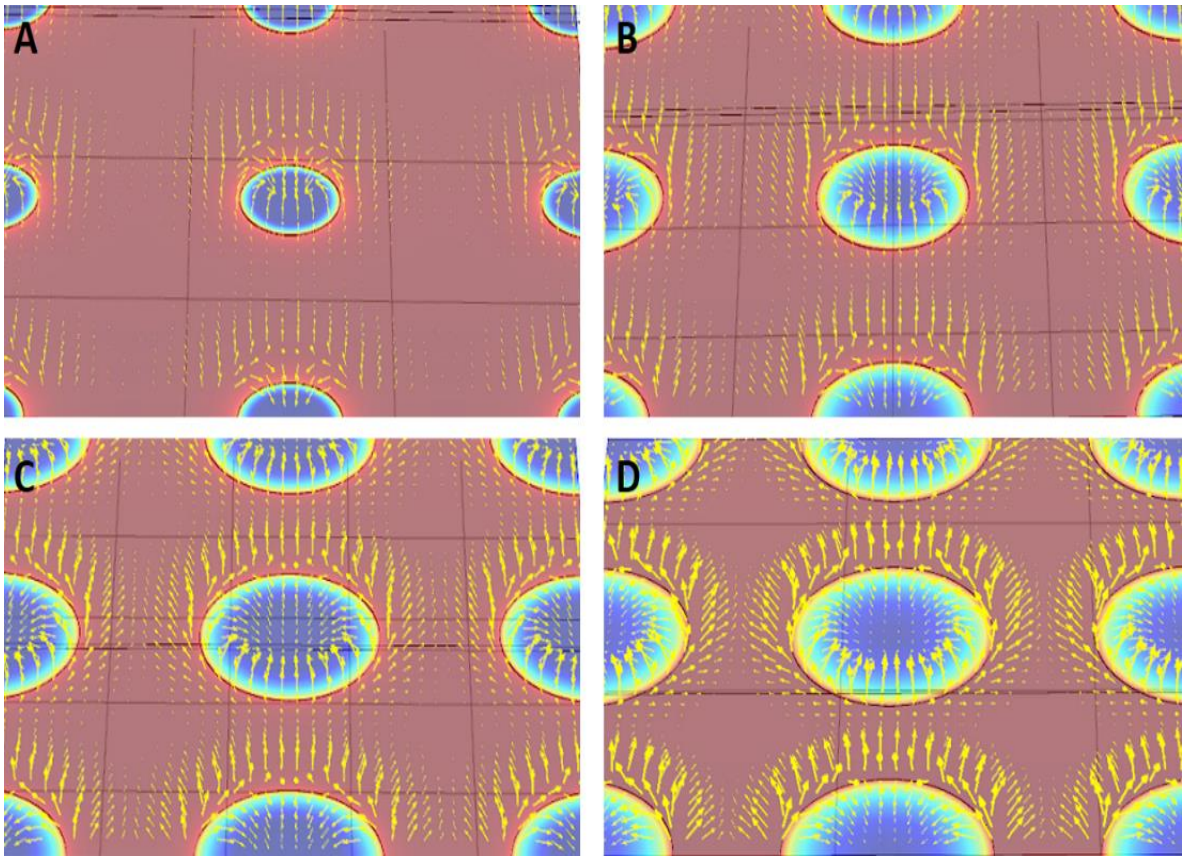

Figure 22. Direction and strength of negative DEP force that exerts on a particle depending on the size of the trap: (A) 10 μm; (B) 20 μm; (C) 30 μm; (D) 40 μm. The strongest DEP force occurs at the rim towards the center of the trap in all sizes. However, The DEP force at the center decreases as the trap size increase, while the repulsive force around the rim increases as the trap size increase.

The direction and strength of negative DEP force in Figure 22 were converted to a line graph as shown in Figure 23. Each graph shows the values of DEP force in X-axis and Z-axis according to the location of the trap. These Force-Distance line graphs explain the several unique properties of the DEP trap such as the repulsive force, the strongest force at the rim, and the weak force at the center in more detail.

First of all, the repulsive force around the rim was more developed as the trap size increased. It could be examined considering the X-axis forces that exert towards the opposite direction of the X-axis forces in the trap. For example, X-axis force in the 10 μm trap was almost equal to zero until it became to have a meaningful value near the rim and it meant the trap didn't have any repulsive force. In the opposite, X-axis force in the 40 μm trap reached to about -4.0×10^{-10} N outside the rim and this force exerts outwards the rim.

Secondly, the strongest force occurred at the rim and it increased as the trap size increased. The strongest X-axis force in the 10 μm ~ 40 μm trap was measured as 3.5×10^{-10} N, 4.6×10^{-10} N, 5.9×10^{-10} N, and 8.3×10^{-10} N respectively.

Lastly, both X-axis and Z-axis force at the center decreased as the trap size increased. It was notable that the bigger traps had weaker forces inside the trap even though these traps had stronger forces around the rim. To be specific, X-axis force was zero in all traps. However, Z-axis force was not zero even at the center of the trap and it was supposed to drag particles downwards considering that the value was negative.

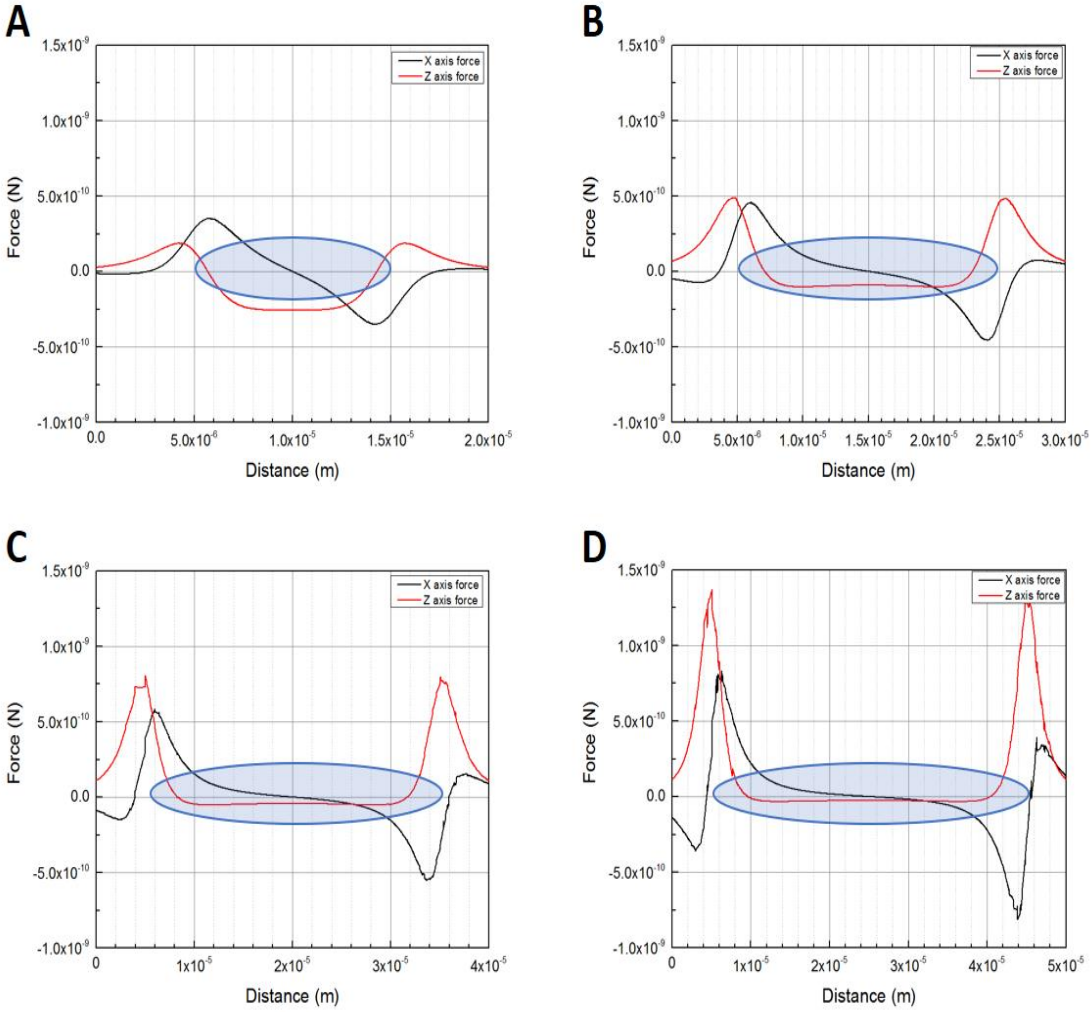

Figure 23. Line graphs of negative DEP force in X-axis and Z-axis depending on the size of the trap: (A) 10 μm; (B) 20 μm; (C) 30 μm; (D) 40 μm. The transparent circle represents the size of the trap. Both X-axis and Z-axis force around the rim increase as the trap size increases from 10 μm to 40 μm. However, the absolute value of Z-axis force and the effect of X-axis force at the center decease as the trap size increases. It also demonstrates that the repulsive force around the rim increases according to the size of trap.

Trapping experiment on the same condition as the numerical method was performed to match the numerical results to the experimental results. Applied frequency was set as 1MHz to generate negative DEP. Applied voltage and trap size were changed from 5 V to 8 V and from 10 μm to 40 μm respectively to see differences of the DEP force field according to the applied voltage and the trap size. The gap between adjacent traps was fixed as 20 μm and the gap between the bottom electrodes and the upper ITO was kept as 30 μm using a 30 μm thickness double-sided tape. 4 μm polystyrene bead was used as a particle and the conductivity of the bead solution was controlled between 3 μS/cm to 5 μS/cm to minimize a difference of each experimental condition. To acquire reliable data, the high-speed camera's frame duration was set from 30 frame/sec to 50 frame/sec depending on the speed of particles.

16 sets of experiment in total were conducted varying applied voltages and trap sizes. First, a distance between the edge of trap and the center of captured particle was measured to analyze correlation between velocity and captured location. In each experimental set, the velocity of 20 particles was obtained. The velocity was acquired by calculating traveled distance and consumed time for the travel. As shown in Figure 24, the trapped location inside the trap showed a close relation with particle's velocity. Particles with lower velocity were captured closer to the center of trap in all sizes, while particles with higher velocity were trapped closer to the rim of trap. This experimental results proved that high speed particles needed much forces that exert opposite the direction of moving particle until they were fully stopped. The relationship between captured location and particle's velocity showed a linear relationship.

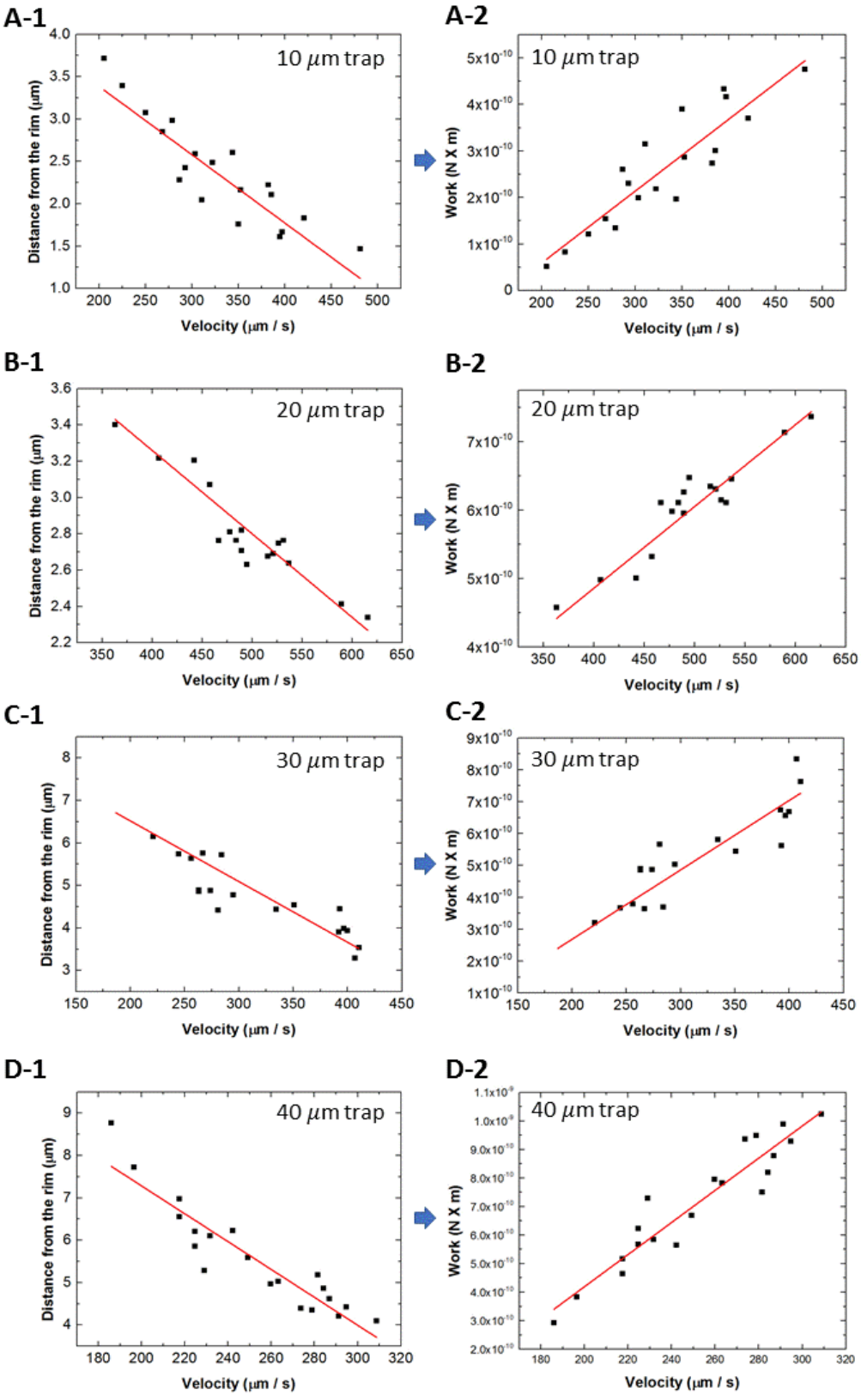
A-1
10 μm trap
Distance from the rim (μm)
Velocity (μm / s)
A-2
10 μm trap
Work (N X m)
Velocity (μm / s)
B-1
20 μm trap
Distance from the rim (μm)
Velocity (μm / s)
B-2
20 μm trap
Work (N X m)
Velocity (μm / s)
C-1
30 μm trap
Distance from the rim (μm)
Velocity (μm / s)
C-2
30 μm trap
Work (N X m)
Velocity (μm / s)
D-1
40 μm trap
Distance from the rim (μm)
Velocity (μm / s)
D-2
40 μm trap
Work (N X m)
Velocity (μm / s)

Figure 24. Correlation between trapped location and velocity and correlation between work and velocity when 8 V is applied. Both type of graphs shows a linear relationship. Particles with lower velocity are captured closer to the center of trap in all sizes, while particles with higher velocity are trapped closer to the rim of trap. In the same way, more work is needed to capture a faster particle. It is worth noting the transition of graphs from A-1, B-1, C-1, and D-1 to A-2, B-2, C-2, and D-2 enables to quantifying the DEP trap properties to measure a particle's kinetic energy in terms of force and work.

The graphs of A-1, B-1, C-1, and D-1 in Figure 24 were transferred to A-2, B-2, C-2, and D-2 respectively combining the numerical method results with the experimental method results. In particular, the concept of "work" was applied to analyze the correlation between the particle's velocity and the trap's influence because the DEP force at the location of trapped particle didn't mean that the particle was captured due to the DEP force itself. However, work could explain how much a total force was needed to fully stop the moving particle. For example, one moving particle that was captured at the 2.0 μm from the edge of trap needed the integrated force from the center of trap to the point where it was trapped as shown in Figure 25, which was the concept of "work".

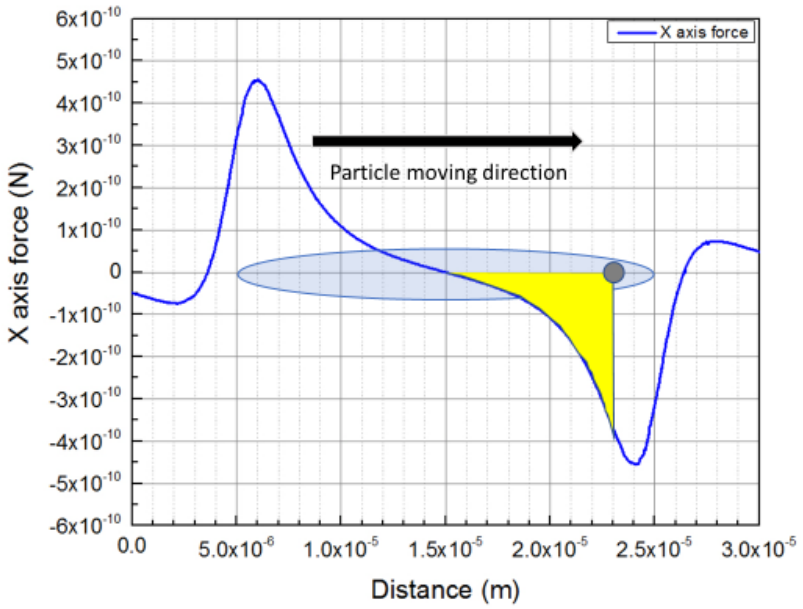

Figure 25. Introduction of work to analyzing the relation of particle velocity and DEP trap effectiveness. When the moving particle is captured at the 2.0 μm from the edge of trap, the needed work to fully stop the moving particle is calculated by integrating the forces from the center of trap to the captured location as the area marked yellow in the graph.

Interestingly, the relation of the needed work and the particle velocity showed a linear relationship too as shown in Figure 24. To capture a faster particle, more work was needed. Above of all, the transition of graphs from A-1, B-1, C-1, and D-1 to A-2, B-2, C-2, and D-2 enabled to quantifying the DEP trap properties to measure a particle's kinetic energy in terms of force and work.

All velocity-work graphs under 5 V ~ 8 V was combined into one graph for further analysis. Figure 26 shows the correlation between work and velocity in the 10 μm, 20 μm, 30 μm, and 40 μm trap. Each line graph showed linear relation between velocity and work. However, any of these lines overlapped resulting in different values of work to capture the same speed particle. For example, 2.0×10^{-10} N × m was needed to capture a particle with 300 μm / s

in the 10 μm trap, while 3.9×10^{-10} N × m, 5.1×10^{-10} N × m, and 7.0×10^{-10} N × m were needed in the 20 μm, 30 μm, and 40 μm trap respectively. This result could be demonstrated with the combination of X-axis and Z-axis force in the trap. As mentioned above in Figure 23, each size trap had different kinds of graph shape in terms of X-axis and Z-axis force. The 10 μm trap had the strongest Z-axis force inside the trap even though it showed the weakest X-axis force. In the opposite, the 40 μm trap had the weakest Z-axis force inside the trap even though it showed the strongest X-axis force. It suggested that Z-axis played an important role by seizing a moving particle to the bottom of trap leading to a higher efficiency of trapping particle.

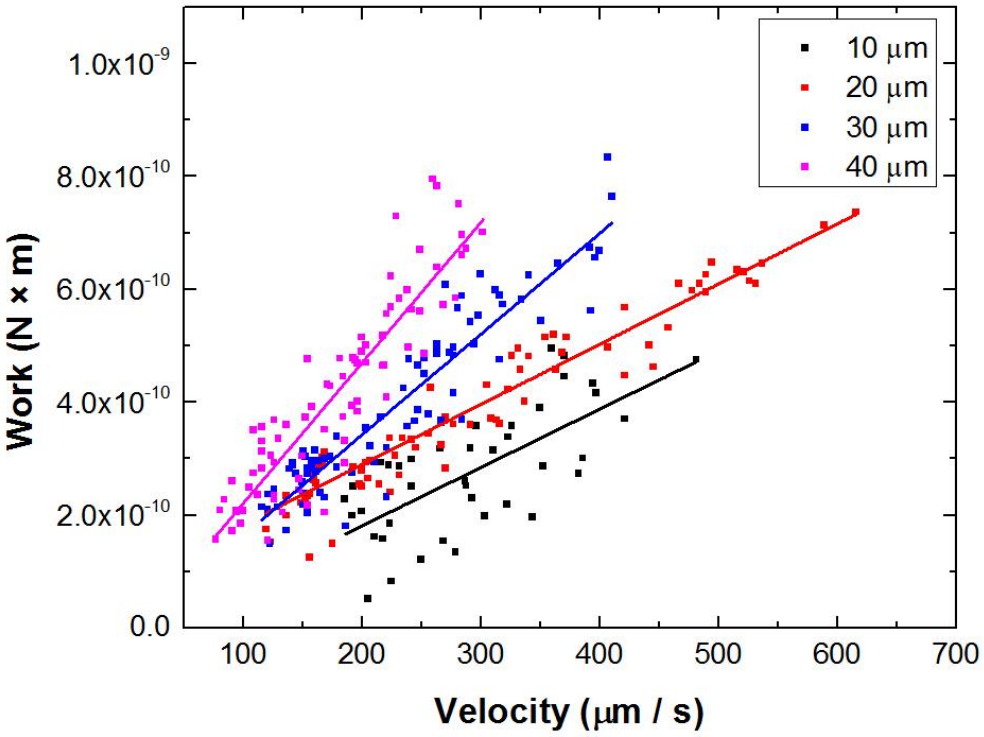

Figure 26. Work-Velocity graphs of each size of trap. The 10 μm trap needs the smallest work to capture the same speed particle, while the 40 μm trap needs the largest work. The effectiveness of trap is related to Z-axis force inside the trap. In terms of the velocities of captured particle,

the 20 μm trap captures the highest velocity particle up to 620 μm / s. This characteristic is also related to the interaction between X-axis and Z-axis force inside the trap.

Since the gap between the bottom electrodes and the upper ITO was kept as 30 μm using a 30 μm thickness double-sided tape, the center of 4 μm bead had enough space to be located from 2 μm to 28 μm in terms of the Z-axis. It meant that Z-axis forces in Figure 23 could affect a moving particle by lifting and pulling it. Z-axis force in each trap tended to lift a particle around the rim, while it tended to pull the particle inside the trap according to the graphs generated by the numerical method. This phenomenon was also observed in the experiments.

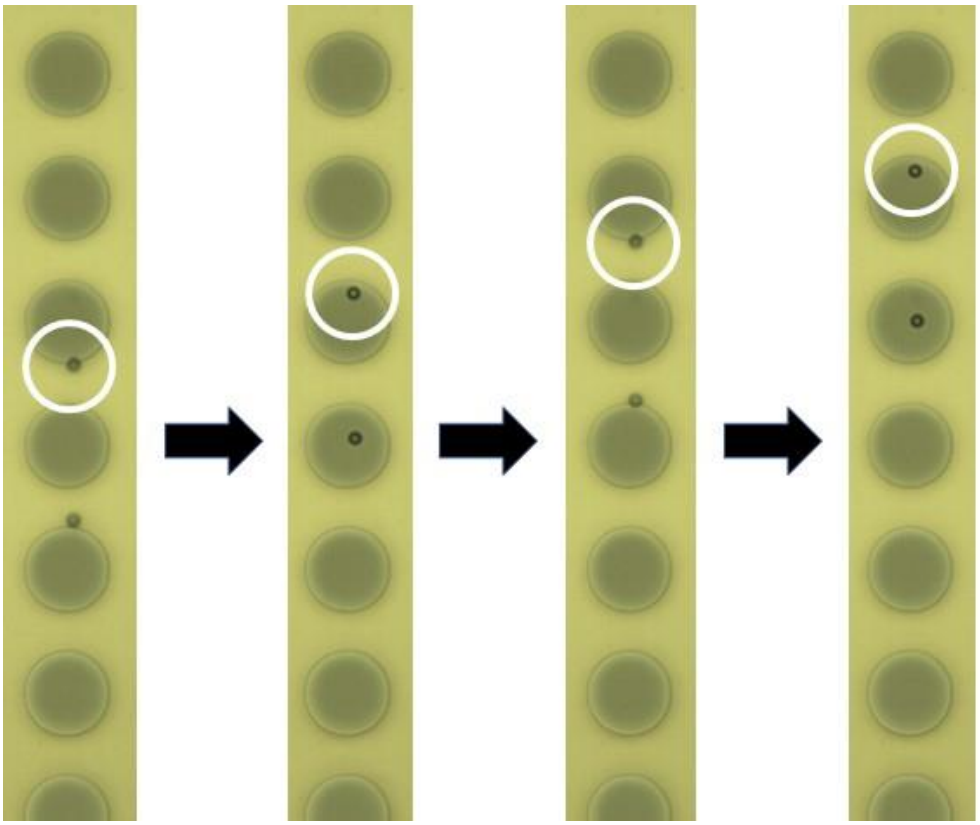

Figure 27. Four consecutive particle trapping pictures. When the particle inside the white circle was levitated by Z-axis that exerted upwards, it became blurry. In contrast, when the particle was traveled right above the electrode by Z-axis that exerted downwards, it showed clear shape with white circular center. It demonstrated that the moving particle was affected not only X-axis force but also Z-axis force. This experiment showed a great agreement with the computer simulation.

Four consecutive particle trapping pictures were taken with the high-speed camera as shown in Figure 27. One particle inside the white circle moved through the circular traps without being trapped due to its high speed exceeding the limit to be captured. The microscope focused on the bottom layer. When the particle traveled along the bottom electrodes, it showed clear shape of the particle and white center inside the particle. In the opposite, when the particle traveled floating from the bottom, it shoed blurry shape and the white center inside the trap became unnoticeable. This resolution-related micro scope technique for observing levitation of particles has been studied and proved [44]. In Figure 27, it was observed that the particle kept repeating to be blurry and clear. When the particle was located around the rim, it became unclear and the white center disappeared, which meant the particle was levitated. In contrast, when the particle was located inside the trap, it became clear and the white center appeared again. It demonstrated the particle was attached to the bottom electrodes because of Z-axis that exerted downwards.

X-axis force played a major role to trap a moving particle and the required work to capture the particle was derived from the integration of X-axis force. At the same time, Z-axis force played a supportive role to seize the particle towards the bottom electrodes leading to a

higher trapping efficiency. In Figure 26, the 10 μm trap showed the highest trapping efficiency by trapping a 300 μm / s particle with only 2.0×10^{-10} N × m due to its strongest Z-axis force inside the trap among the 10 μm ~ 40 μm trap. In contrast, the 40 μm trap showed the lowest trapping efficiency by trapping a 300 μm / s particle with only 7.0×10^{-10} N × m due to its weakest Z-axis force inside the trap. After all, it was concluded that the efficiency of trap was arranged from 10 μm to 40 μm in accordance with the strength of Z-axis force inside the trap.

One of the most important and notable results was that the fastest velocity of the captured particles in each trap was not in order of trap size. The fastest velocity of the captured particles in the trap of 10 μm to 40 μm was 481 μm / s, 615 μm / s, 410 μm / s, and 308 μm / s respectively. This velocity data could be put in order of trap size resulting in the sequence of 20 $\mu m \rightarrow$ 10 $\mu m \rightarrow$ 30 $\mu m \rightarrow$ 40 μm. This sequence didn't reflect simply either the power of X-axis force inside the trap or the efficiency of the trap originated from Z-axis force. The strength of X-axis force that played a major role in trapping a particle was in order of the 40 $\mu m \rightarrow$ 30 $\mu m \rightarrow$ 20 $\mu m \rightarrow$ 10 μm trap. On the contrary, the strength of Z-axis force that enhanced the efficiency of trapping particles was in order of the 10 $\mu m \rightarrow$ 20 $\mu m \rightarrow$ 30 $\mu m \rightarrow$ 40 μm trap.

The new sequence of the traps that were arranged in order of the fastest velocity of the captured particles was the result of the interaction between X-axis and Z-axis force inside the trap. Figure 28 shows how much X-axis force exerted on a particle at the location where Z-axis force became negative to positive. This location was the spot where a particle started to levitate under the effect of Z-axis force. In the analysis of "Work-velocity graphs of each size of trap" in Figure 26 and "Four consecutive particle trapping pictures" in Figure 27, it was already demonstrated that particle traveled up and down under the effect of Z-axis force. In case of the

20 μm trap, Z-axis force became negative to positive at 2.1 μm from the edge of the trap, which was 7.1 μm distance in the graph of B in Figure 28. At the location, 3.6^{-10} N of X-axis force exerted on a particle. Since no particle was captured beyond this point, it could be concluded that particles were no longer captured once it started to levitate and 3.6^{-10} N was the strongest X-axis force that was used to capture the moving particle. Theoretically, DEP force on a particle drastically drops when the particle is away from electrodes and that's the reason no particles was captured right after the particle started to be lifted. It was both numerically and experimentally proved using the same design of the DEP trap in this thesis. In this case, the most adjacent captured particles near the 7.1 μm distance were 7.412 μm and 7.340 μm distance, which were 0.414 μm and 0.340 μm closer to the center of trap compared to the levitation location. At the location of 3.2 μm from the edge of the trap, Z-axis force became negative to positive in the 30 μm trap. It was 8.2 μm distance in the graph of C and 3.0^{-10} N X-axis force was supposed to push back a moving particle to stop. In this case, 8.2877 μm and 8.5396 μm distance were the closest location of the captured particles to 8.2 μm distance. No particle was captured beyond this levitation point. In case of the 40 μm trap, 2.6^{-10} N was the strongest X-axis force that could be used to trap a particle in accordance with the levitation point.

The 10 μm trap showed a unique property compared to other size traps. The levitation point was 5.7 μm distance in the graph of A in Figure 28 and X-axis force at the point was 3.5^{-10} N. However, the fastest particles were captured at 6.403 μm and 6.467 μm distance, which didn't show good agreement with the properties of the rest sizes of trap. In this case, particles couldn't be captured around the levitation point because a big portion of particle was already out of the trap even before the particle reached the levitation point. The particle's radius was 2 μm and the levitation point was only 0.7 μm inside the edge of the 10 μm trap. As a result, the

particles could be captured in the 10 μm trap when a large portion of particle was still inside trap and the last point was 6.403 μm distance according to experiment. At the point, the exerted X-axis force was 3.1^{-10} N.

When the exerted X-axis force at each levitation point and at the location where the fastest particles were trapped in case of the 10 μm trap were put in order of strength, the sequence was 3.6^{-10} N, 3.1^{-10} N, 3.0^{-10} N, and 2.6-10 N in conformity with the order of trap size from 20 μm to 10 μm to 30 μm to 40 μm. This sequence exactly conformed to the result of "Work-velocity graphs of each size of trap" in Figure 26.

This trapping experiment with various sizes of traps proved that X-axis force was the main factor to capture a moving particle and it could be quantified using the concept of work. In addition, Z-axis force affected to the efficiency of the trap by pulling a particle closer to the electrodes where a particle could be under the strongest DEP force. The order of traps that could trap the fastest particles could be explained through the combination effect of X-axis and Z-axis force. It was notable that the levitation point was the important factor deciding a location where was the fastest particle could be captured in case a particle was still inside a trap.

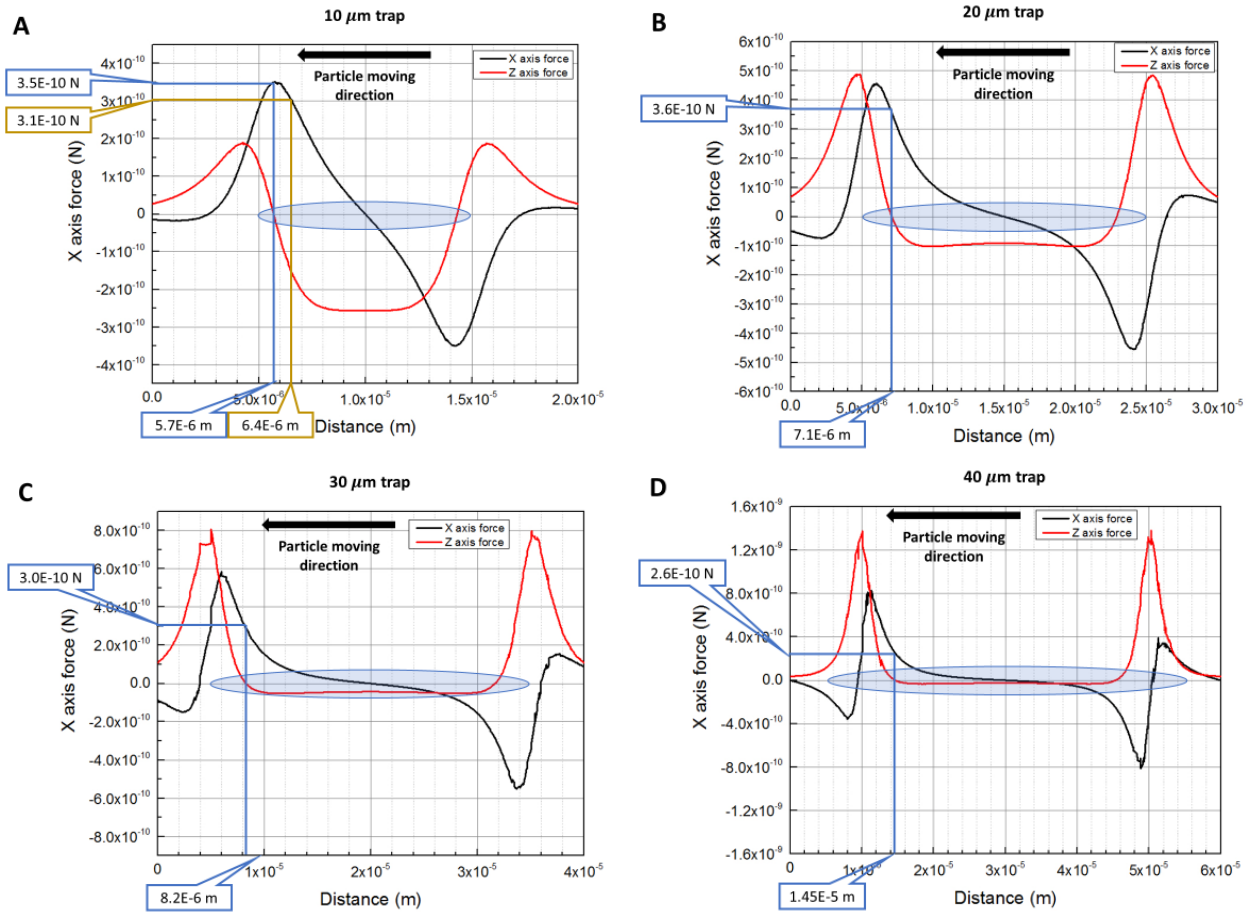

Figure 28. Levitation point of a particle and corresponding X-axis force in each size trap: (A) 10 μm trap; (B) 20 μm trap; (C) 30 μm trap; (D) 40 μm trap. The fastest particles are captured around the levitation point where Z-axis force becomes negative to positive. In case of the 10 μm trap, the fastest particles are captured before the levitation point because a large portion of particle is out of the trap before it reaches the point. The order of the strength of X-axis force at the levitation point decides which trap can capture a faster particle.

4.3 Trapping various sizes of beads

Experiment of trapping various sizes of beads was conducted to see the effect of particle size under the same trap and condition. Computer simulation was also conducted to quantify work that was needed to trap a particle. Applied frequency was set as 1MHz to generate negative DEP. Applied voltage and trap size were set as 8V and 40 μm respectively to control the rest of conditions except particle sizes. The gap between adjacent traps was fixed as 40 μm and the gap between the bottom electrodes and the upper ITO was kept as 30 μm using a 30 μm thickness double-sided tape. 2 μm, 4 μm, 6 μm, and 10 μm polystyrene beads were used as a particle and the conductivity of the bead solution was controlled between 3 μS/cm to 5 μS/cm to minimize a difference of each experimental condition. To acquire reliable data, the high-speed camera's frame duration was set for 50 frame/sec.

4 sets of experiment in total were conducted varying particle size. In a similar way to the previous experiment, the velocity was acquired by calculating traveled distance and consumed time for the travel. In each experimental set, the velocity of 20 particles was obtained. Required work to trap a particle was derived by matching a trapped location inside trap with corresponding numerical force data from computer simulation. Needed work to fully stop a moving particle was calculated by integrating forces from the center of trap to a captured location in the same way as the previous experiment.

Work-velocity graph was made from the velocities of particle and required work to trap a particle as shown in Figure 29. Bigger particles could be captured with higher velocities. 10 μm particle could be trapped with the velocity of up to 1494 μm/s, while 6 μm particle, 4 μm particle, and 2 μm particle could be captured with the velocity of up to 814 μm/s, 442 μm/s, and

147 μm/s respectively. In a similar trend, trapping bigger particles needed more work to be captured due to their high velocity. 8.7^{-8} N was required to trap the fastest 10 μm particle and 2.14^{-8} N, 9.4^{-9} N, 9.2^{-10} N were required to capture the fastest 6 μm, 4 μm, 2 μm particle respectively. This result was in great agreement with a second-degree polynomial equation line resulting in 0.93997 of R-Square value. It could be explained with the fact that DEP force has a close association with particle radius. As mentioned in Equation 1, DEP force increases in connection with the third power of particle radius.

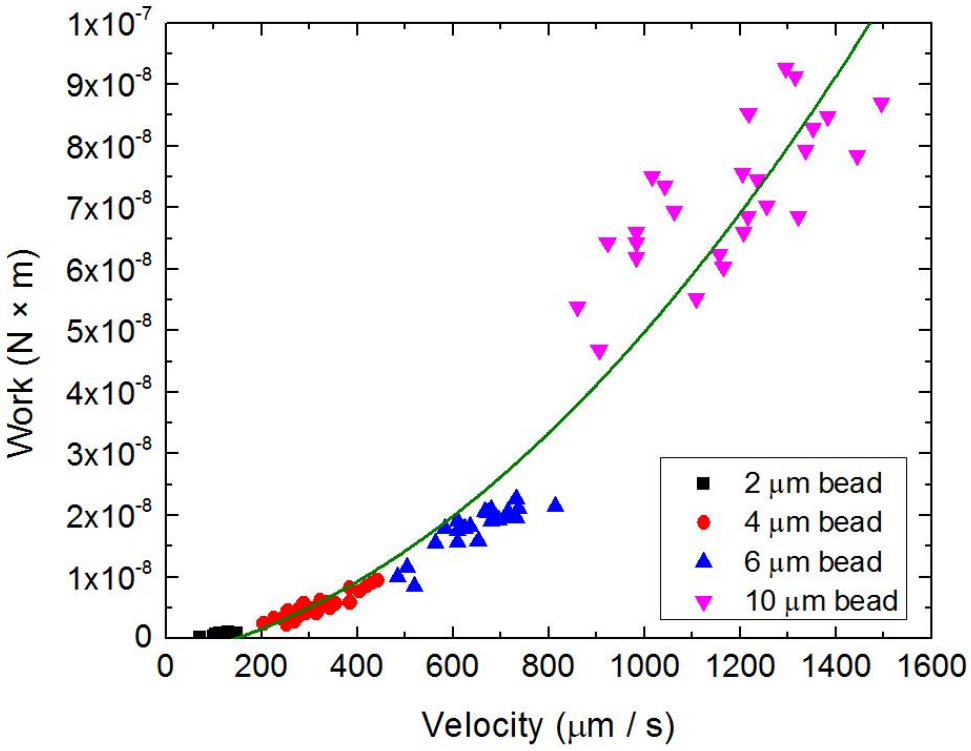

Figure 29. Work-velocity graph of various sizes of beads. Bigger particles are captured with higher velocities. Consumed work to trap bigger particles are also greater than consumed work

to trap smaller particles. It shows good agreement between the experiment and the governing equation of DEP force.

In this experiment, different sizes of particle were captured in different velocity areas. Velocity of captured 10 μm particles ranged from 900 μm/s to 1600 μm/s, while velocity of captured 6 μm, 4 μm, and 2 μm particles ranged from 500 μm/s to 800 μm/s, 200 μm/s to 450 μm/s, and 50 μm/s to 150 μm/s respectively. None of each area overlapped and this result suggested a possibility of different sized particle separation using velocity difference, which will be discussed in the following section.

4.4 Separation of various sizes of beads

Combination effect of X-axis, Z-axis force, and the thickness of spacer offers several ways for particles to travel. Figure 30 shows how a particle can be captured inside the trap or avoid the trap. Particles were trapped in two cases. One case was that a particle was lifted by Z-axis force at the edge avoiding the repulsive force around the rim and dragged down once it entered the trap as A in Figure 30. The other case was when a particle traveled at the proper height to avoid the repulsive force. The particle could be dragged down by Z-axis force at the rim without any effect of repulsive force as B in Figure 30.

Untrapped particles also showed two kinds of movements. When a particle didn't even have enough velocity to approach to the rim, the repulsive force pushed it around and the particle passed along the circular trap as C in Figure 30. The other case was that a particle traveled too far from the electrodes as D in Figure 30. Since DEP force power decrease as a particle is away

from electrodes, any X-axis and Z-axis force can affect a particle. The last and most simple reason was a particle was so fast to pass through the trap.

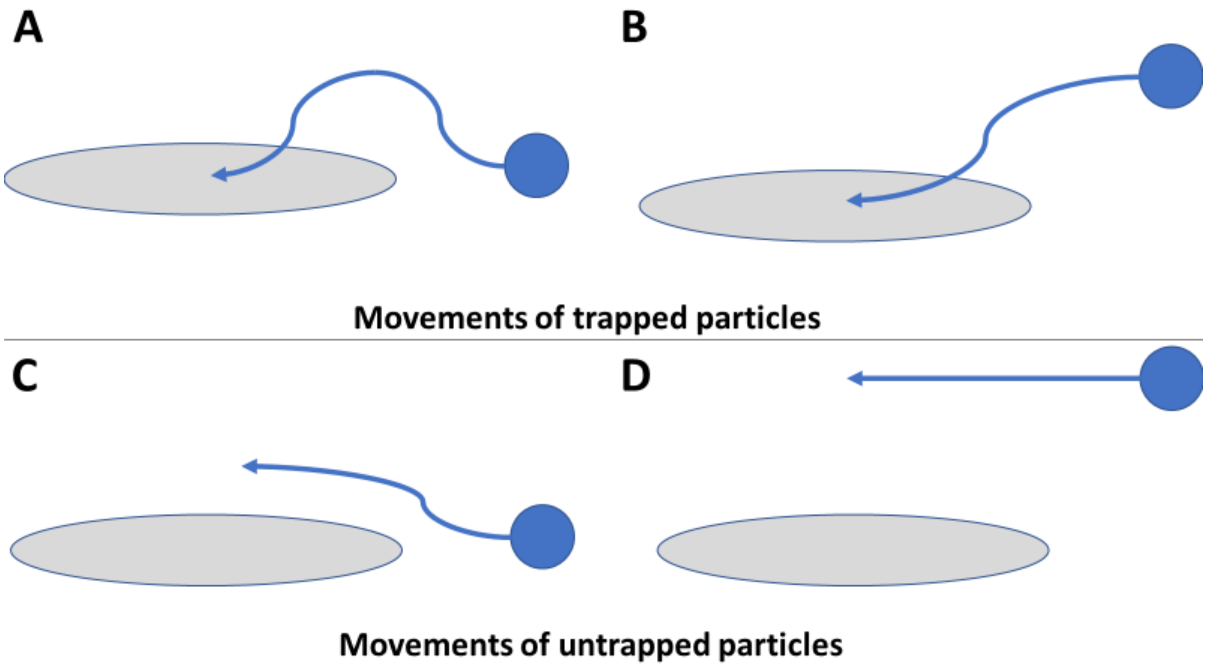

Figure 30. Schematic diagram of particle's movements around and inside the trap: (A) A particle moves up and down by Z-axis force; (B) A particle are dragged down by Z-axis force; (C) A particle is repelled from the trap by repulsive X-axis force; (D) A particle is not affected by any DEP force due to its height.

In particular, the repulsive X-axis force played a major role in separating different sizes of particles. Since bigger particles are affected by stronger DEP force, it is possible for smaller particles to enter the trap as opposed to bigger particle that are repelled from the trap by repulsive X-axis force when these two different sized particles travel with the same speed. This phenomenon is well observed in Figure 31. In these consecutive pictures, several particles approach the trap with a slow velocity that is not enough to get to the edge of trap. When

particles are located near the edge, the repulsive force that occurs around the rim repels particles away and these particles move along the edge of trap.

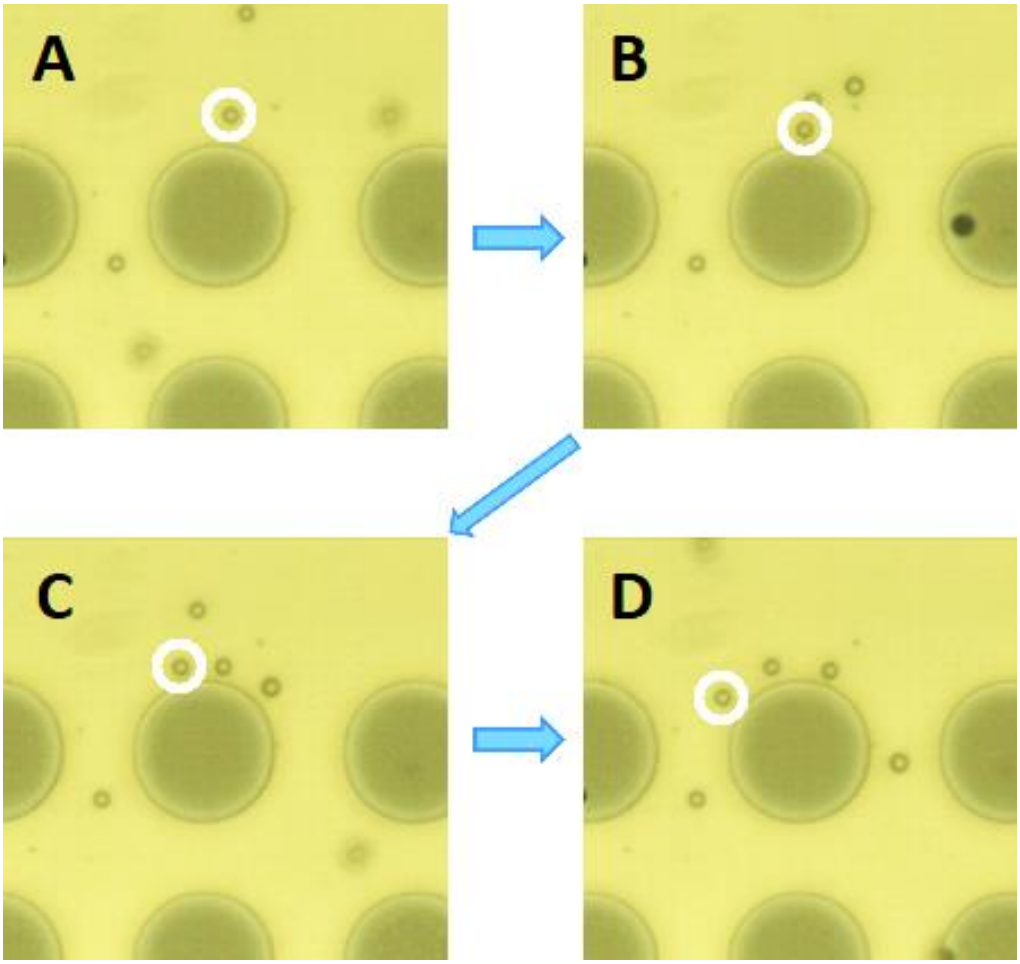

Figure 31. Four consecutive pictures of the effect of repulsive force around the edge. Particles with not enough velocity to approach the edge of trap are repelled away by repulsive X-axis force around the rim.

Using these particles unique movements, 4 μm and 6 μm particles were successfully separated as shown in Figure 32. 4 μm and 6 μm particles were mixed together in the same medium and flowed with different flow rate and applied voltages to match an optimized

condition for trapping each size of particles. When 4 μm particles were separated from 6 μm particles, the flow rate was set as 4 μml/min and 11 V was applied. In a similar way, 6 μm particles were separated from 4 μm particles when the flow rate was set as 7 μml/min and 14 V was applied. These conditions varied depending on a size of channel of LOC. However, the higher flow rate and voltages were required to separate bigger particles. It was because bigger particles could be trapped by a greater DEP force due to its radius even though smaller particles just pass through traps.

When 4 μm particles were separated, 6 μm particles couldn't be captured because of two reasons. One reason was that 6 μm particles were not fast enough to overcome the repulsive force around the rim and get to the edge of trap like C in Figure 30. The other reason was that 6 μm particles traveled too high to be dragged down like D in Figure 30. White circle in A in Figure 32 showed a 6 μm particle traveled above the trap since it was out of the effect of DEP force. Since the focus of a microscope was at the electrodes, particles that traveled away from the electrodes were observed blurry as opposed to trapped particles that were distinct.

In case of 6 μm particle separation, the mechanism was different from the 4 μm particle separation even though it also had two reasons 4 μm couldn't be trapped. First reason was the same as one of the reasons of 4 μm separation. When 4 μm particles traveled too high away from the electrode, it couldn't be trapped as shown in the yellow circle in B in Figure 32. The other reason was that 4 μm particles were too fast to be captured. A enough amount of velocity was required for 6 μm particles to overcome the repulsive force around the rim and get inside the trap. Since 4 μm particles also traveled with the same flow rate as 6 μm particles, this velocity was fast enough for 4 μm particles to pass through the traps.

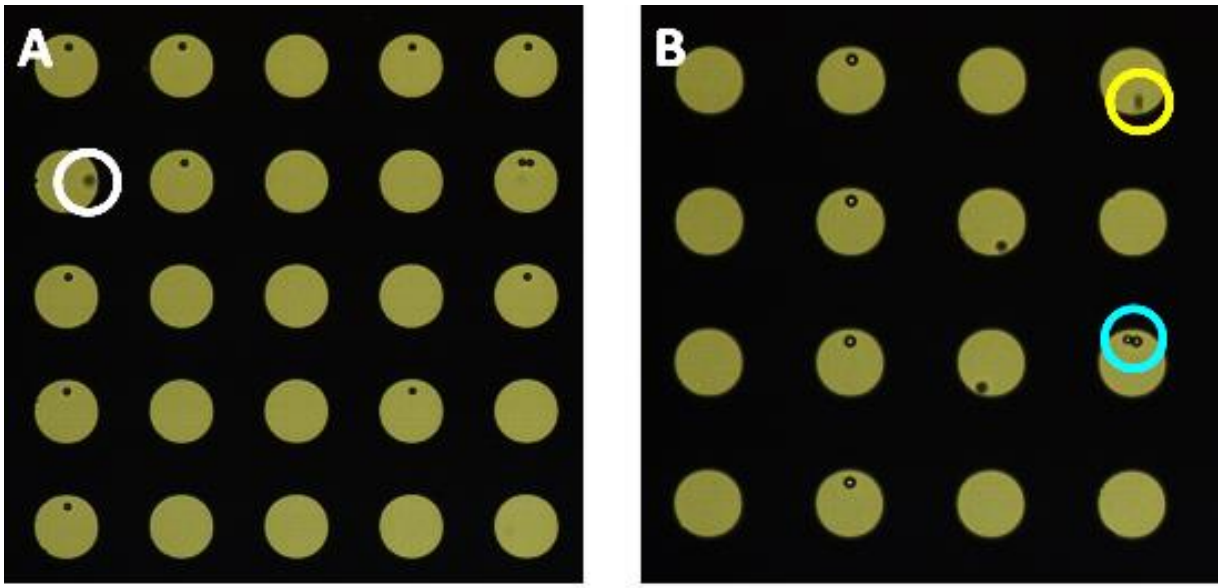

Figure 32. 4 µm and 6 µm particle separation from the mix of 4 µm and 6 µm particles: (A) 4 µm particle separation; (B) 6 µm particle separation. In the left picture, 4 µm particles can be separated because either 6 µm particles are too slow or travel too high from the electrodes. White circle shows a 6 µm particle that is traveling far from the bottom. In the right picture, 6 µm particles can be separated because either 4 µm particles are too fast or travel too high from the electrodes. Yellow circle shows a 4 µm particle traveling too fast and passing through trap. Blue circle shows the size comparison between 4 µm and 6 µm particle.

Chapter 5

Conclusion

5.1 Overall summary

In the thesis, an array of circular dielectrophoresis (DEP) traps was developed and tested to manipulate population of microparticles in single particle level. The circular DEP traps enabled more precise control of the force field than conventionally used interdigitated electrodes due to its omnidirectional and symmetric properties. The location of the captured microparticle inside the trap was confirmed by both of numerical and experimental approaches, based on the direction and amplitude of the force field generated by numerical simulation.

A single particle was successfully captured inside the suggested DEP trap and a particle's physical properties such as speed and required work to be captured were also derived based on both of numerical and experimental approaches. In particular, particle's movement inside the trap system was thoroughly analyzed and several different types of capturing mechanism were established. Due to the comprehensive understanding of the particle movements, different sizes of mixed particles were successfully separated. The individual microparticle captured in separate trap can be further tested or treated by follow up treatments.

5.2 Future direction

The suggested DEP trap can be applied to living cells for further experiments and the success of follow up experiments and treatments will result in two novel techniques. One technique is separation of cells. As a separation of mixed particles was already proven, living

cells are expected to be filtered or separated. For example, a specific type of cell can be segregated from whole blood due to a different permittivity or size of cell.

Secondly, the motility of the biological cells such as sperm and E. coli will be measured. Each sperm in separate trap can be analyzed for each cell's specific motility including speed and force to capture. The operation condition, applied frequency and voltage will be optimized to quantitatively compare the sperm motility. Trapped sperm's moving and swimming force required to escape a trap can be derived based on the measurement of applied DEP force. Consequently, this can contribute clinical fertility treatments by supplying standardized tool to quantitatively sort strong sperm. Similar concept can be combined with chemotaxis to provide strong driving force of motility to many living cells. For example, E. coli has a tendency to move toward favorable locations with high concentrations of attractants (amino acids and sugars) and avoid repellents (commonly poisons). The change of the concentration of attractants and repellents around trap is expected to control motility of E. coli. The results can be used to quantitatively compare the attractants and repellents.

REFERENCES

[1] T. Lilliehorn *et al.*, “Trapping of microparticles in the near field of an ultrasonic transducer,” *Ultrasonics*, vol. 43, no. 5, pp. 293–303, Mar. 2005.

[2] S.-B. Huang *et al.*, “High-purity and label-free isolation of circulating tumor cells (CTCs) in a microfluidic platform by using optically-induced-dielectrophoretic (ODEP) force,” *Lab. Chip*, vol. 13, no. 7, pp. 1371–1383, 2013.

[3] M. Tanyeri and C. M. Schroeder, “Manipulation and Confinement of Single Particles Using Fluid Flow,” *Nano Lett.*, vol. 13, no. 6, pp. 2357–2364, Jun. 2013.

[4] J. Shah and E. Wilkins, “Electrochemical Biosensors for Detection of Biological Warfare Agents,” *Electroanalysis*, vol. 15, no. 3, pp. 157–167, Mar. 2003.

[5] E.-M. Laux, U. C. Kaletta, F. F. Bier, C. Wenger, and R. Hölzel, “Functionality of dielectrophoretically immobilized enzyme molecules,” *ELECTROPHORESIS*, vol. 35, no. 4, pp. 459–466, Feb. 2014.

[6] L.-C. Hsiung *et al.*, “Dielectrophoresis -based cellular microarray chip for anticancer drug screening in perfusion microenvironments,” *Lab. Chip*, vol. 11, no. 14, pp. 2333–2342, 2011.

[7] C. S. Ivanoff, T. L. Hottel, and F. Garcia-Godoy, “Dielectrophoresis: A model to transport drugs directly into teeth,” *ELECTROPHORESIS*, vol. 33, no. 8, pp. 1311–1321, Apr. 2012.

[8] H. A. Pohl and J. S. Crane, “Dielectrophoresis of Cells,” *Biophys. J.*, vol. 11, no. 9, pp. 711–727, Sep. 1971.

[9] H. A. Pohl and J. S. Crane, “Dielectrophoretic force,” *J. Theor. Biol.*, vol. 37, no. 1, pp. 1–13, Oct. 1972.

[10] B. Yafouz, N. A. Kadri, and F. Ibrahim, “Dielectrophoretic Manipulation and Separation of Microparticles Using Microarray Dot Electrodes,” *Sensors*, vol. 14, no. 4, pp. 6356–6369, Apr. 2014.

[11] R. Pethig and G. H. Markx, “Applications of dielectrophoresis in biotechnology,” *Trends Biotechnol.*, vol. 15, no. 10, pp. 426–432, Oct. 1997.

[12] M. P. Hughes, H. Morgan, and F. J. Rixon, “Measuring the dielectric properties of herpes simplex virus type 1 virions with dielectrophoresis,” *Biochim. Biophys. Acta BBA - Gen. Subj.*, vol. 1571, no. 1, pp. 1–8, May 2002.

[13] B. Yafouz, N. A. Kadri, and F. Ibrahim, “Microarray Dot Electrodes Utilizing Dielectrophoresis for Cell Characterization,” *Sensors*, vol. 13, no. 7, pp. 9029–9046, Jul. 2013.

[14] K. Khoshmanesh *et al.*, “Dielectrophoretic manipulation and separation of microparticles using curved microelectrodes,” *ELECTROPHORESIS*, vol. 30, no. 21, pp. 3707–3717, Nov. 2009.

[15] C. Qian *et al.*, “Dielectrophoresis for Bioparticle Manipulation,” *Int. J. Mol. Sci.*, vol. 15, no. 10, pp. 18281–18309, Oct. 2014.

[16] R. Hamada, H. Takayama, Y. Shonishi, L. Mao, M. Nakano, and J. Suehiro, “A rapid bacteria detection technique utilizing impedance measurement combined with positive and negative dielectrophoresis,” *Sens. Actuators B Chem.*, vol. 181, pp. 439–445, May 2013.

[17] M. P. Hughes, H. Morgan, F. J. Rixon, J. P. H. Burt, and R. Pethig, “Manipulation of herpes simplex virus type 1 by dielectrophoresis,” *Biochim. Biophys. Acta BBA - Gen. Subj.*, vol. 1425, no. 1, pp. 119–126, Sep. 1998.

[18] R. Martinez-Duarte, F. Camacho-Alanis, P. Renaud, and A. Ros, “Dielectrophoresis of lambda-DNA using 3D carbon electrodes,” *ELECTROPHORESIS*, vol. 34, no. 7, pp. 1113–1122, Apr. 2013.

[19] “Microfluidic separation of live and dead yeast cells using reservoir-based dielectrophoresis,” *Biomicrofluidics*, vol. 6, no. 3, p. 034102, Jul. 2012.

[20] A. Menachery *et al.*, “Counterflow Dielectrophoresis for Trypanosome Enrichment and Detection in Blood,” *Sci. Rep.*, vol. 2, p. 775, Oct. 2012.

[21] E. Rosales-Cruzaley, P. A. Cota-Elizondo, D. Sánchez, and B. H. Lapizco-Encinas, “Sperm cells manipulation employing dielectrophoresis,” *Bioprocess Biosyst. Eng.*, vol. 36, no. 10, pp. 1353–1362, Oct. 2012.

[22] C.-H. Chuang, Y.-W. Huang, and Y.-T. Wu, “System-Level Biochip for Impedance Sensing and Programmable Manipulation of Bladder Cancer Cells,” *Sensors*, vol. 11, no. 11, pp. 11021–11035, Nov. 2011.

[23] X. B. Wang, Y. Huang, X. Wang, F. F. Becker, and P. R. Gascoyne, “Dielectrophoretic manipulation of cells with spiral electrodes,” *Biophys. J.*, vol. 72, no. 4, pp. 1887–1899, Apr. 1997.

[24] H. O. Fatoyinbo, K. F. Hoettges, and M. P. Hughes, “Rapid-on-chip determination of dielectric properties of biological cells using imaging techniques in a dielectrophoresis dot microsystem,” *ELECTROPHORESIS*, vol. 29, no. 1, pp. 3–10, Jan. 2008.

[25] L. Liu, X. Ye, K. Wu, R. Han, Z. Zhou, and T. Cui, “Humidity Sensitivity of Multi-Walled Carbon Nanotube Networks Deposited by Dielectrophoresis,” *Sensors*, vol. 9, no. 3, pp. 1714–1721, Mar. 2009.

[26] M. S. Pommer *et al.*, “Dielectrophoretic separation of platelets from diluted whole blood in microfluidic channels,” *ELECTROPHORESIS*, vol. 29, no. 6, pp. 1213–1218, Mar. 2008.

[27] C. Iliescu, L. Yu, F. E. H. Tay, and B. Chen, “Bidirectional field-flow particle separation method in a dielectrophoretic chip with 3D electrodes,” *Sens. Actuators B Chem.*, vol. 129, no. 1, pp. 491–496, Jan. 2008.

[28] L. Wang, J. Lu, S. A. Marchenko, E. S. Monuki, L. A. Flanagan, and A. P. Lee, “Dual frequency dielectrophoresis with interdigitated sidewall electrodes for microfluidic flow-through separation of beads and cells,” *ELECTROPHORESIS*, vol. 30, no. 5, pp. 782–791, Mar. 2009.

[29] M. Dürr, J. Kentsch, T. Müller, T. Schnelle, and M. Stelzle, “Microdevices for manipulation and accumulation of micro- and nanoparticles by dielectrophoresis,” *ELECTROPHORESIS*, vol. 24, no. 4, pp. 722–731, Feb. 2003.

[30] R. S. Thomas, H. Morgan, and N. G. Green, “Negative DEP traps for single cell immobilisation,” *Lab. Chip*, vol. 9, no. 11, pp. 1534–1540, 2009.

[31] K. F. Hoettges, Y. Hübner, L. M. Broche, S. L. Ogin, G. E. N. Kass, and M. P. Hughes, “Dielectrophoresis-Activated Multiwell Plate for Label-Free High-Throughput Drug Assessment,” *Anal. Chem.*, vol. 80, no. 6, pp. 2063–2068, Mar. 2008.

[32] M. Son *et al.*, “Characterization of the Stiffness of Multiple Particles Trapped by Dielectrophoretic Tweezers in a Microfluidic Device,” *Langmuir*, vol. 32, no. 3, pp. 922–927, Jan. 2016.

[33] R. Pethig, Y. Huang, X. Wang, and J. P. H. Burt, “Positive and negative dielectrophoretic collection of colloidal particles using interdigitated castellated microelectrodes,” *J. Phys. Appl. Phys.*, vol. 25, no. 5, p. 881, 1992.

[34] H. Rezaei Nejad, O. Z. Chowdhury, M. D. Buat, and M. Hoorfar, “Characterization of the geometry of negative dielectrophoresis traps for particle immobilization in digital microfluidic platforms,” *Lab. Chip*, vol. 13, no. 9, pp. 1823–1830, 2013.

[35] N. Lewpiriyawong and C. Yang, “Continuous separation of multiple particles by negative and positive dielectrophoresis in a modified H-filter,” *ELECTROPHORESIS*, vol. 35, no. 5, pp. 714–720, Mar. 2014.

[36] J. Voldman, R. A. Braff, M. Toner, M. L. Gray, and M. A. Schmidt, “Holding Forces of Single-Particle Dielectrophoretic Traps,” *Biophys. J.*, vol. 80, no. 1, pp. 531–542, Jan. 2001.

[37] H. Yin and D. Marshall, “Microfluidics for single cell analysis,” *Curr. Opin. Biotechnol.*, vol. 23, no. 1, pp. 110–119, Feb. 2012.

[38] F. Gs and C. Dt, “Disposable microfluidic devices: fabrication, function, and application.,” *BioTechniques*, vol. 38, no. 3, pp. 429–446, Mar. 2005.

[39] M. Ritzi-Lehnert, “Development of chip-compatible sample preparation for diagnosis of infectious diseases,” *Expert Rev. Mol. Diagn.*, vol. 12, no. 2, pp. 189–206, Mar. 2012.

[40] M. L. Sin, J. Gao, J. C. Liao, and P. K. Wong, “System Integration - A Major Step toward Lab on a Chip,” *J. Biol. Eng.*, vol. 5, p. 6, 2011.

[41] S. Masuda, M. Washizu, and T. Nanba, “Novel method of cell fusion in field constriction area in fluid integration circuit,” *IEEE Trans. Ind. Appl.*, vol. 25, no. 4, pp. 732–737, Jul. 1989.

[42] H. Tian, J. Shao, Y. Ding, X. Li, and X. Li, “Numerical studies of electrically induced pattern formation by coupling liquid dielectrophoresis and two-phase flow,” *ELECTROPHORESIS*, vol. 32, no. 17, pp. 2245–2252, Sep. 2011.

[43] M. Li, S. Li, W. Li, W. Wen, and G. Alici, “Continuous manipulation and separation of particles using combined obstacle- and curvature-induced direct current dielectrophoresis,” *ELECTROPHORESIS*, vol. 34, no. 7, pp. 952–960, Apr. 2013.

[44] I. S. Park *et al.*, “Biaxial Dielectrophoresis Force Spectroscopy: A Stoichiometric Approach for Examining Intermolecular Weak Binding Interactions,” *ACS Nano*, vol. 10, no. 4, pp. 4011–4019, Apr. 2016.

[45] M. G. S. Ferreira, M. Da Cunha Belo, N. E. Hakiki, G. Goodlet, M. F. Montemor, and A. M. P. Simões, “Semiconducting properties of oxide and passive films formed on AISI 304 stainless steel and Alloy 600,” *J. Braz. Chem. Soc.*, vol. 13, no. 4, pp. 433–440, Aug. 2002.